TU Delft

Delft University of Technology

Reducing parameter tuning in topology optimization of flow problems using a Darcy and Forchheimer penalization

Theulings, M. J.B.; Noël, L.; Langelaar, M.; Maas, R.

DOI
10.1016/j.cma.2025.118027

Publication date
2025

Document Version
Final published version

Published in
Computer Methods in Applied Mechanics and Engineering

Citation (APA)
Theulings, M. J. B., Noël, L., Langelaar, M., & Maas, R. (2025). Reducing parameter tuning in topology optimization of flow problems using a Darcy and Forchheimer penalization. *Computer Methods in Applied Mechanics and Engineering*, *443*, Article 118027. https://doi.org/10.1016/j.cma.2025.118027

Important note
To cite this publication, please use the final published version (if applicable).
Please check the document version above.

Copyright
Other than for strictly personal use, it is not permitted to download, forward or distribute the text or part of it, without the consent of the author(s) and/or copyright holder(s), unless the work is under an open content license such as Creative Commons.

Takedown policy
Please contact us and provide details if you believe this document breaches copyrights.
We will remove access to the work immediately and investigate your claim.

This work is downloaded from Delft University of Technology.
For technical reasons the number of authors shown on this cover page is limited to a maximum of 10.

Computer Methods in Applied Mechanics and Engineering 443 (2025) 118027

Contents lists available at ScienceDirect

Comput. Methods Appl. Mech. Engrg.

journal homepage: www.elsevier.com/locate/cma

Reducing parameter tuning in topology optimization of flow problems using a Darcy and Forchheimer penalization

M.J.B. Theulings [a,b,*], L. Noël [a], M. Langelaar [a], R. Maas [b]

[a] Delft University of Technology, Delft, The Netherlands
[b] Royal Netherlands Aerospace Centre, Amsterdam, The Netherlands

ARTICLE INFO

Keywords:
Density-based topology optimization
Laminar flow
Forchheimer penalization
Darcy penalization
Parameter selection
Parameter continuation

ABSTRACT

In density-based topology optimization of flow problems, flow in the solid domain is generally inhibited using a penalization approach. Setting an appropriate maximum magnitude for the penalization traditionally requires manual tuning to find an acceptable compromise between flow solution accuracy and design convergence. In this work, three penalization approaches are examined, the Darcy (D), the Darcy with Forchheimer (DF), and the newly proposed Darcy with filtered Forchheimer (DFF) approach. Parameter tuning is reduced by analytically deriving an appropriate penalization magnitude for accuracy of the flow solution. The Forchheimer penalization is found to be required to reliably predict the accuracy of the flow solution. The state-of-the-art D and DF approaches are improved by developing the novel DFF approach, based on a spatial average of the velocity magnitude. In comparison, the parameter selection in the DFF approach is more reliable, as convergence of the flow solution and objective convexity are more predictable. Moreover, a continuation approach on the maximum penalization magnitude is derived by numerical inspection of the convexity of the pressure drop response. Using two-dimensional optimization benchmarks, the DFF approach reliably finds accurate flow solutions and is less prone to converge to inferior local optima.

1. Introduction

Designing flow structures is of importance for many engineering problems, see for example, the design of tesla-type turbine devices [1], microfluidic mixers [2], or drag minimization and lift maximization [3]. Such problems often involve moderate to high Reynolds flow, which is difficult to design for due to the highly nonlinear flow equations. A tool to design flow structures is density-based Topology Optimization (TO). In flow TO, we intend to find an optimal phase distribution to separate a design domain into distinct solid and fluid parts. This is commonly accomplished by introducing the Darcy penalization to inhibit flow in the solid domain [4–6]. High penalizations are present in the solid domain, low or no penalizations are used in the fluid domain. A continuous penalization interpolation is used between the solid and the fluid domain, such that gradient-based optimizers can be used. This approach can be seen as an optimization by penalty method [7], where the zero velocity constraint in the solid domain is enforced using a penalty term. In this approach, a proper selection of the magnitude of the penalization is crucial. It is well known that the penalization should be high enough to sufficiently inhibit flow in the solid domain, but small enough to ensure numerical stability. Often, finding the correct penalty requires manual tuning [8], which is time consuming and requires experience with TO. In this work we focus on the flow penalization in TO of moderate Reynolds flow problems, and aim to improve parameter robustness and algorithmic stability.

* Corresponding author at: Delft University of Technology, Delft, The Netherlands.
E-mail address: m.j.b.theulings@tudelft.nl (M.J.B. Theulings).

https://doi.org/10.1016/j.cma.2025.118027
Received 26 January 2025; Received in revised form 21 March 2025; Accepted 15 April 2025
Available online 22 May 2025
0045-7825/© 2025 The Authors. Published by Elsevier B.V. This is an open access article under the CC BY license (http://creativecommons.org/licenses/by/4.0/).

The most common approach to select an appropriate magnitude for the Darcy penalization is presented by Olesen et al. [6]. The maximum penalization is determined based on a Darcy number and a characteristic length L. As a characteristic length the inlet diameter is often used, and in porous flow modeling, the Darcy number relates viscous and porous friction forces. However, parameter tuning remains necessary to select a Darcy number, such that flow is sufficiently reduced in the solid domain. On top of a user-defined Darcy number, [3] include the Reynolds number to select the maximum penalty magnitude, and recent work confirms that the relation between flow reduction and penalization depends on the Reynolds number for inertia dominated flows [9]. However, complex geometries with locally varying flow velocities, length scales, and Reynolds numbers may be found using TO. A Darcy penalization based on a *single* estimation of the Reynolds number is thus unable to appropriately penalize flow in all parts of a design.

As the Darcy penalization is linearly dependent on the velocity magnitude, including the Reynolds number in the penalization results in a penalization which depends quadratically on velocity magnitude. A direct way to include a quadratic dependency on the flow magnitude in the penalty is through the Forchheimer penalization [10]. Alonso and Silva [1] find improved designs when using the Forchheimer penalization in addition to the Darcy penalization. However, selecting the appropriate magnitude for the Forchheimer penalization also requires manual tuning. Often, the maximum penalization magnitude is selected based on the physical interpretation of the Forchheimer term as a friction term for flow through porous media [11–13]. So far, no critical analysis on the relation between Forchheimer penalization and accuracy of the flow solution has been performed.

Flow solutions are obtained using discretization. Bruns [7] selects a penalty which is a couple of magnitudes larger than the largest diagonal stiffness matrix value, which suggests a relation between discretization and penalization magnitude. Recent work by Theulings et al. [14] and by Abdelhamid and Czekanski [15] suggests that the penalization should depend on the mesh size. This is supported by Jensen [16], who finds increasingly thin features using mesh adaptation for increasingly high penalization magnitudes.

Another problem generally associated with the penalty approach is the convergence to ill-performing local optima. Design convergence is influenced by the maximum penalization, the penalty interpolation, and the initial design. Borrvall and Petersson [4] show that a linear interpolation of the Darcy penalization results in optimal discrete solid/fluid designs without intermediate gray areas for Stokes flow problems. However, to escape ill-performing local optima, a penalization interpolation function which lowers the penalty for intermediate *gray* design variables is used in the earlier design iterations. Gersborg-Hansen et al. [5] note that a lower penalization for gray design variables increases the convexity of the objective response, but also increases the amount of gray in the optimal design. A continuation approach which starts with a low penalization for gray design variables to escape ill-performing local optima, and ends with a higher penalization for gray design variables is recommended. Olesen et al. [6] improve the convergence behavior of the design by first optimizing using a low maximum flow penalization, allowing the optimizer to escape ill-performing local optima but finding designs with inaccurate flow solutions. Subsequently, the design is further optimized using a higher maximum penalization, resulting in designs with accurate flow solutions. Moreover, initial designs, dominated by flow penalization, are found to show a larger tendency to converge to ill-performing local optima. The relation between the choice of interpolation function and the objective behavior is analyzed on a simplified problem where a solid/fluid boundary is slightly modified for a fluid structure interaction problem in [17]. Results suggest that the objective should respond monotonically to design updates for the problem to be well-posed. Besides the convergence of the design, the convergence of the flow solution should be taken into account. While using a high flow penalization increases the accuracy of the flow solution, it can affect the stability of the flow solver [18]. The penalization approach should thus be included in the stabilization approach of the flow solver [19].

In this work, we aim to formulate a reliable approach for moderate Reynolds flow TO, which exhibits four desirable traits:

1. Parameter tuning is reduced.
2. The flow solution in the optimized design is accurate.
3. The optimization procedure does not show a tendency to converge to inferior local optima.
4. The flow solver remains stable over changing designs during the optimization process.

To reduce parameter tuning, we closely inspect three different penalization approaches in Section 2, and derive appropriate parameters for the magnitude of the flow penalization. We inspect the common approach using the Darcy penalization, and introduce two new approaches which additionally include the Forchheimer penalization. In Section 3, we discuss the implementation and the stabilization approach for the flow solution. Numerical analyses are performed using the finite element method implemented in [20], as the necessary capabilities are readily available and as the use of a commercial software will further promote the use of presented techniques outside academia. In Section 4, we investigate the accuracy of the flow solution and the robustness of our parameter definition for varying Reynolds numbers. Subsequently, in Section 4.2, we inspect the convexity of the pressure drop objective, and derive a novel continuation strategy. In Section 5, the different approaches are compared in terms of accuracy of the optimized solution and of tendency to converge to inferior local optima for two different TO problems. We evaluate our novel method with respect to the proposed four traits identified for a reliable approach in the discussion in Section 6 and conclude in Section 7.

2. Penalization in laminar flow topology optimization

In this section, we introduce the incompressible Navier–Stokes equations used to model laminar flows. To make them suitable for density-based TO and represent fluid and solid, we add penalization terms. Several approaches including Darcy and/or Forchheimer penalizations are explored. To derive an appropriate penalization magnitude, we use a dimensional analysis similar to [14]. In

Section 2.2, the novel approach to the dimensional analysis will lead to the same results found by Theulings et al. [14], confirming its validity. In Section 2.3, we introduce the Forchheimer penalization similar to [1] and use our method to derive novel settings for the penalization magnitudes of this term. Finally, in Section 2.4, we introduce a novel approach based on the Forchheimer penalization and a filtered velocity magnitude and derive the associated appropriate penalization magnitudes.

2.1. Incompressible Navier–Stokes equations for density-based TO

For laminar flow problems, the steady-state incompressible Navier–Stokes equations consist of: (i) the momentum equation, which represents the forces acting on an infinitesimal volume of fluid, and (ii) the continuity equation, which ensures that no fluid mass is created or destroyed. They are given in residual form as:

$$\begin{aligned} \boldsymbol{R}_{\mathbf{v}}(\mathbf{v},p) &= -\rho\nabla\mathbf{v}\cdot\mathbf{v} - \nabla p + \nabla\cdot\left(\mu\left(\nabla\mathbf{v}+\nabla\mathbf{v}^{\top}\right)\right) = \mathbf{0}, \\ R_p(\mathbf{v}) &= \nabla\cdot\mathbf{v} = 0, \end{aligned} \tag{1}$$

where $\mathbf{v}^{\top} = [u, v]$ is the velocity vector with u and v, the velocities in x and y direction, p the pressure field, ρ the fluid density, and μ the dynamic viscosity. In the momentum equation, we find the inertial force $\rho\nabla\mathbf{v}\cdot\mathbf{v}$, the pressure force $-\nabla p$, and the viscous force $\nabla\cdot\left(\mu\left(\nabla\mathbf{v}+\nabla\mathbf{v}^{\top}\right)\right)$.

For density-based TO, a design variable α, representing the fluid volume fraction, is used to distinguish between solid and fluid parts of the design domain. We continuously interpolate between the solid domain, $\alpha = 0$, and the fluid domain, $\alpha = 1$. In the solid domain, we aim to inhibit the flow by counteracting the forces in the momentum equation. The most common approach to adapt the Navier–Stokes equations to density-based TO is through the Darcy penalization [4–6], here referred to as the D approach, which adds a force proportional to and in the opposite direction of the velocity to the momentum equation:

$$\boldsymbol{R}_{\mathbf{v}}(\mathbf{v},p) = -\rho\nabla\mathbf{v}\cdot\mathbf{v} - \nabla p + \nabla\cdot\left(\mu\left(\nabla\mathbf{v}+\nabla\mathbf{v}^{\top}\right)\right) \overbrace{-D_1(\alpha)\mathbf{v}}^{\text{Darcy penalization}} = \mathbf{0}. \tag{2}$$

where $D_1(\alpha)$ is a design dependent interpolation which inhibits flow in the solid domain using a high penalization $D_1(\alpha = 0) = \overline{D}_1$. The flow is governed by the standard momentum equation and $D_1(\alpha = 1) = 0$ in the fluid domain. The challenge in this adaptation lies in the selection of an appropriate maximum value $\overline{D}_1$ and of an adequate interpolation function $D_1(\alpha)$. The maximum penalization $\overline{D}_1$ should be large enough to sufficiently penalize the flow in the solid domain. However, it should not be chosen too large, as such a choice would lead to a deterioration of the convergence of the forward solution due to ill-conditioning of the system equations, as well as a premature convergence to ill-performing local optima.

To define an appropriate magnitude for the penalization, we follow a similar approach to our earlier work [14] and investigate the local flow reduction. Flow reduction is defined as the ratio v^s/v^f between v^s and v^f, the flow magnitudes in neighboring solid and fluid domains, respectively. We intend to define the maximum penalization $\overline{D}_1$ such that we can accurately predict $v^s/v^f = 10^{-q}$, where the user-defined parameter q indicates the order of magnitude by which the velocity in the solid and fluid domain differ. Subsequently, we can select the parameter q and the interpolation function $D_1(\alpha)$ to achieve a compromise between accuracy and convergence.

The flow reduction should be appropriate in the smallest scale represented by our model, i.e., the expected flow reduction is achieved in the thinnest design features. In this work, we use the finite element method to discretize the Navier–Stokes equations. We derive penalization magnitudes in the context of this discretization, although the proposed derivation is not limited to the finite element method and can be applied for other weighted residual methods, such as the finite volume method. To estimate the flow reduction, we consider a small part of the design domain Ω^P, discretized with four square elements of size h, as shown in Fig. 1. We define a fluid domain Ω^f, made of two fluid elements, and a solid domain Ω^s, made of two solid elements. The interface between fluid and solid is defined as $\Gamma = \Omega^f \cap \Omega^s$. We aim to define a penalization such that $v^s/v^f = 10^{-q}$, where the velocity magnitude v^f represents the maximum magnitude in fluid elements neighboring solid elements with a velocity magnitude v^s.

The discretized residual is used to compare the velocity magnitudes v^s and v^f. From the discretization in Fig. 1, we select the center Node P on the interface to which test function $\phi^P(\boldsymbol{x})$ is attached, with $\boldsymbol{x}^{\top} = [x, y]$ the spatial coordinate vector. In the finite element discretization, the test function spans only the four elements in $\Omega^P = \Omega^f \cup \Omega^s$ which are attached to Node P and are zero outside of Ω^P and on the boundary $\Gamma^P = \overline{\Omega^P} \setminus \Omega^P$. The weighted residuals attached to Node P in domain Ω^P, are subsequently defined using the discretized velocity and pressure fields $\mathbf{v}^h(\boldsymbol{x})$ and $p^h(\boldsymbol{x})$:

$$\begin{bmatrix} R_u^P \\ R_v^P \end{bmatrix} = \int_{\Omega^P} \phi^P \boldsymbol{R}_{\mathbf{v}}(\mathbf{v}^h, p^h) d\Omega = \int_{\Omega^f} \phi^P \boldsymbol{R}_{\mathbf{v}}(\mathbf{v}^h, p^h) d\Omega + \int_{\Omega^s} \phi^P \boldsymbol{R}_{\mathbf{v}}(\mathbf{v}^h, p^h) d\Omega = \mathbf{0}, \tag{3}$$

where we defined the discretized residuals R_u^P and R_v^P, in x and y direction respectively, using the same scalar test function ϕ^P. In the finite element method, weighted residuals of the momentum equation are commonly defined per element and subsequently assembled in the complete residual $\boldsymbol{R}_{\mathbf{v}}^h = \mathbf{0}$, discretized on the N_d nodes in the mesh. For this analysis, we investigate all contributions to Node P at once, associated with the complete residual as $\boldsymbol{R}_{\mathbf{v}}^{h\top} = [R_u^1, R_v^1, \ldots, R_u^P, R_v^p, \ldots, R_u^{N_d}, R_v^{N_d}] = \mathbf{0}$.

Eq. (3) presents the weighted residual of the momentum equation at Node P in the solid/fluid domain Ω^P. For the discretized residual to be zero, we require the discretized solid and fluid domain terms to be in equilibrium. Using Eq. (3), we will be able to compare the velocity magnitudes v^f and v^s in the neighboring fluid and solid elements.

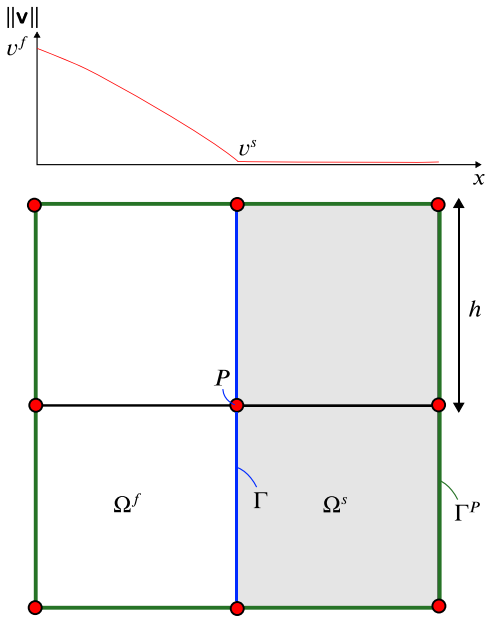

Fig. 1. A four element domain Ω^P, with two fluid elements ($\alpha = 1$) to the left in Ω^f (white) and two solid elements ($\alpha = 0$) to the right in Ω^s (gray), such that $\Omega^P = \Omega^f \cup \Omega^s$ with boundary $\Gamma^P = \overline{\Omega^P} \setminus \Omega^P$. At the solid/fluid interface $\Gamma = \Omega^f \cap \Omega^s$, node P is selected for the analysis of flow leakage. On top the behavior of the flow magnitude over the elements is illustrated. In the fluid domain Ω^f we find a flow magnitude $\|\mathbf{v}\| = v^f$ which decreases towards $\|\mathbf{v}\| = v^s$ at the solid/fluid interface Γ after which it stagnates at a magnitude v^s in the solid domain Ω^s. We assume a regular mesh with elements of size h.

We use the fact that for Eq. (3) to hold, the fluid and solid domain terms on the right-hand side are equal in magnitude and opposite in direction:

$$\left| \int_{\Omega^s} \phi^P \boldsymbol{R}_{\mathbf{v}}(\mathbf{v}^h, p^h) d\Omega \right|_2 = \left| \int_{\Omega^f} \phi^P \boldsymbol{R}_{\mathbf{v}}(\mathbf{v}^h, p^h) d\Omega \right|_2, \tag{4}$$

where $|\square|_2$ is the L^2-norm. We proceed to approximate the terms in Eq. (4) using approximate fluid and solid domain velocity magnitudes v^f and v^s. First, we simplify the required analysis. If $|\boldsymbol{R}_{\mathbf{v}}(\mathbf{v}^h, p^h)|_2 = C$ is constant, the left- and right-hand side in Eq. (4) become $\left|\int_{\Omega^s} \phi^P d\Omega\right|_2 C$ and $\left|\int_{\Omega^f} \phi^P d\Omega\right|_2 C$, respectively. We use the test function ϕ^P to inspect the residual at Node P, but do not want to approximate its value and aim for the derivation to be general and independent on a specific test function. We thus normalize Eq. (4) as:

$$\frac{\left|\int_{\Omega^s} \phi^P \boldsymbol{R}_{\mathbf{v}}(\mathbf{v}^h, p^h) d\Omega\right|_2}{\left|\int_{\Omega^s} \phi^P d\Omega\right|_2} = \frac{\left|\int_{\Omega^f} \phi^P \boldsymbol{R}(\mathbf{v}^h, p^h)_{\mathbf{v}} d\Omega\right|_2}{\left|\int_{\Omega^f} \phi^P d\Omega\right|_2}. \tag{5}$$

We note that due to the symmetry of ϕ^P over Γ and the structured square mesh, $\left|\int_{\Omega^s} \phi^P d\Omega\right|_2 = \left|\int_{\Omega^f} \phi^P d\Omega\right|_2$. If a different unstructured mesh is used, this normalization does not hold and the difference in element size and shape in the fluid and solid domains has to be taken into account. Subsequently, we define a notation for approximating the orders of magnitude of the residuals as:

$$\mathcal{O}^s\left(\boldsymbol{R}_{\mathbf{v}}\right) \approx \frac{\left|\int_{\Omega^s} \phi^P \boldsymbol{R}_{\mathbf{v}}(\mathbf{v}^h, p^h) d\Omega\right|_2}{\left|\int_{\Omega^s} \phi^P d\Omega\right|_2}, \qquad \mathcal{O}^f\left(\boldsymbol{R}_{\mathbf{v}}\right) \approx \frac{\left|\int_{\Omega^f} \phi^P \boldsymbol{R}_{\mathbf{v}}(\mathbf{v}^h, p^h) d\Omega\right|_2}{\left|\int_{\Omega^f} \phi^P d\Omega\right|_2}, \tag{6}$$

which can be approximated and compared as $\mathcal{O}^f\left(\boldsymbol{R}_{\mathbf{v}}\right) \approx \mathcal{O}^s\left(\boldsymbol{R}_{\mathbf{v}}\right)$.

In this paper, we use the following rules for computing approximate orders of magnitude $\mathcal{O}^s(\bullet)$ and $\mathcal{O}^f(\bullet)$. For an arbitrary vector field $\boldsymbol{\Psi}(\boldsymbol{x})$ in Ω^f and Ω^s, we define:

$$\mathcal{O}^s\left(\boldsymbol{\Psi}\right) = \Psi^s, \qquad \mathcal{O}^f\left(\boldsymbol{\Psi}\right) = \Psi^f, \tag{7}$$

where we approximate $\Psi^s \approx |\boldsymbol{\Psi}|_2 \in \Omega^s$ and $\Psi^f \approx |\boldsymbol{\Psi}|_2 \in \Omega^f$. The largest gradient is assumed to be dependent on the element size h such that:

$$\mathcal{O}^s\left(\nabla\boldsymbol{\Psi}\right) \approx \Delta\Psi^s/h, \qquad \mathcal{O}^f\left(\nabla\boldsymbol{\Psi}\right) \approx \Delta\Psi^f/h, \tag{8}$$

where $\Delta\Psi^s$, $\Delta\Psi^f$ are estimates of the *maximum* change of $|\boldsymbol{\Psi}|_2$ in Ω^s and Ω^f, respectively. We emphasize that this assumption on the magnitude of gradients is essential, and can only be made because we investigate the discretized residual in Eq. (3). Using an

analysis of the residual in Eq. (2), gradients would be related to an overall length scale L related to the design, which would lead to the common approach relating the penalization magnitude to a Darcy number Da and L [6], which has limitations as shown by Theulings et al. [14]. Finally, we assume that only one term in either the fluid and solid domain is dominant:

$$\mathcal{O}^s\left(\boldsymbol{A}+\boldsymbol{B}\right) \approx \max\left(\mathcal{O}^s\left(\boldsymbol{A}\right), \mathcal{O}^s\left(\boldsymbol{B}\right)\right), \qquad \mathcal{O}^f\left(\boldsymbol{A}+\boldsymbol{B}\right) \approx \max\left(\mathcal{O}^f\left(\boldsymbol{A}\right), \mathcal{O}^f\left(\boldsymbol{B}\right)\right). \tag{9}$$

To summarize, we use an estimation of $\mathcal{O}^f\left(\boldsymbol{R}_{\mathbf{v}}\right) \approx \mathcal{O}^s\left(\boldsymbol{R}_{\mathbf{v}}\right)$ to derive an approximation for v^s/v^f. This is done by examining each term in $\boldsymbol{R}_{\mathbf{v}}(\mathbf{v}^h, p^h)$, as presented in Eq. (2), individually. Subsequently, the approximation is used to define a penalization such that we achieve a desired flow reduction $v^s/v^f = 10^{-q}$.

2.2. The Darcy approach

First, we examine how to appropriately use the D approach and study its limitations. We start by investigating the magnitude of the terms in the fluid domain Ω^f. The magnitude of the velocity gradient is approximated using the plot in Fig. 1. We find a velocity magnitude of $\left|\mathbf{v}^h\right|_2 = v^f$ on the left edge of Ω^f and of $\left|\mathbf{v}^h\right|_2 = v^s \ll v^f$ on the right edge of Ω^f at the solid/fluid interface Γ. In Ω^f we assume that any change in velocity magnitude between neighboring nodes in the fluid domain is lower than between fluid and neighboring solid/fluid interface nodes. Consequently, the maximum change in velocity magnitude is approximated as $\Delta v^f = v^f - v^s \approx v^f$. As square elements are used, the maximum velocity gradient is found in the direction normal to the fluid/solid interface Γ, and is approximated as $\mathcal{O}^f\left(\nabla\mathbf{v}^h\right) \approx \Delta v^f/h \approx v^f/h$. We note that for distorted elements with high aspect ratios, this assumption may not hold. The magnitude of the inertial and viscous terms are consequently approximated as:

$$\mathcal{O}^f\left(-\rho\nabla\mathbf{v}^h\cdot\mathbf{v}^h + \nabla\cdot\left(\mu\left(\nabla\mathbf{v}^h + \nabla\mathbf{v}^{h\top}\right)\right)\right) \approx \max\left(\rho\frac{{v^f}^2}{h}, \mu\frac{v^f}{h^2}\right). \tag{10}$$

Subsequently, the magnitude of the pressure term is approximated as:

$$\mathcal{O}^f\left(\nabla p^h\right) \approx \frac{\Delta p^f}{h}, \tag{11}$$

where Δp^f is an estimate of the maximum change in pressure in Ω^f. In the fluid domain the magnitude of the Darcy penalization is zero, $D_1(\alpha = 1) = 0$. Finally, the magnitude of the terms in the fluid domain can be estimated as:

$$\mathcal{O}^f\left(\boldsymbol{R}_{\mathbf{v}}\right) \approx \max\left(\rho\frac{{v^f}^2}{h}, \mu\frac{v^f}{h^2}, \frac{\Delta p^f}{h}\right). \tag{12}$$

The magnitude of the velocity gradient in the solid domain is estimated using the change in velocity Δv^s as $\mathcal{O}^s\left(\nabla\mathbf{v}^h\right) \approx \Delta v^s/h$, which is used to approximate the inertial and viscous terms:

$$\mathcal{O}^s\left(-\rho\nabla\mathbf{v}^h\cdot\mathbf{v}^h + \nabla\cdot\left(\mu\left(\nabla\mathbf{v}^h + \nabla\mathbf{v}^{h\top}\right)\right)\right) \approx \max\left(\rho\frac{v^s\Delta v^s}{h}, \mu\frac{\Delta v^s}{h^2}\right). \tag{13}$$

Similar to the fluid domain, we approximate the pressure term as:

$$\mathcal{O}^s\left(\nabla p^h\right) \approx \frac{\Delta p^s}{h}, \tag{14}$$

In the solid domain, the magnitude of the Darcy penalization is maximal, $D_1(\alpha = 0) = \overline{D}_1$, and is estimated as:

$$\mathcal{O}^s\left(D_1(\alpha)\mathbf{v}^h\right) \approx \overline{D}_1 v^s. \tag{15}$$

Gathering terms from Eqs. (13), (14), (15), the magnitude of the terms in the solid domain is estimated as:

$$\mathcal{O}^s\left(\boldsymbol{R}_{\mathbf{v}}\right) \approx \max\left(\rho\frac{v^s\Delta v^s}{h}, \frac{\Delta p^s}{h}, \mu\frac{\Delta v^s}{h^2}, \overline{D}_1 v^s\right). \tag{16}$$

As we assume that the terms in the fluid and solid domain are in equilibrium $\mathcal{O}^f\left(\boldsymbol{R}_{\mathbf{v}}\right) \approx \mathcal{O}^s\left(\boldsymbol{R}_{\mathbf{v}}\right)$:

$$\max\left(\rho\frac{{v^f}^2}{h}, \frac{\Delta p^f}{h}, \mu\frac{v^f}{h^2}\right) \approx \max\left(\rho\frac{v^s\Delta v^s}{h}, \frac{\Delta p^s}{h}, \mu\frac{\Delta v^s}{h^2}, \overline{D}_1 v^s\right). \tag{17}$$

Our approach is to investigate each term on the left-hand side assuming it is dominant. Subsequently, we investigate how the right-hand side counteracts these terms and how the velocity magnitudes are related. A first working assumption is that if an appropriate penalization is applied then $v^f \gg v^s > \Delta v^s$. Since the inertial and viscous terms scale the same with respect to ρ, μ and h in the fluid and solid domains, we neglect the solid domain inertial and viscous terms as they cannot counteract the fluid domain terms. Reducing Eq. (17) to:

$$\max\left(\rho\frac{{v^f}^2}{h}, \frac{\Delta p^f}{h}, \mu\frac{v^f}{h^2}\right) \approx \max\left(\frac{\Delta p^s}{h}, \overline{D}_1 v^s\right). \tag{18}$$

Moreover, in [14] we derived an appropriate penalization based on the assumption that the pressure field is C^1-continuous and $\mathcal{O}^s\left(\nabla p^h\right) \approx \mathcal{O}^f\left(\nabla p^h\right)$. In [21] and from experience, we find this assumption to hold across a solid/fluid interface. Assuming that if dominant, the pressure gradients are in equilibrium, we neglect them in the order analysis:

$$\max\left(\rho\frac{{v^f}^2}{h}, \mu\frac{v^f}{h^2}\right) \approx \overline{D}_1 v^s. \tag{19}$$

In Eq. (19), two terms might be dominant in the fluid domain. We need to determine which one to select an appropriate maximum penalization $\overline{D}_1$. Following [14], we select the dominant term based on the elemental Reynolds number, the ratio between elemental inertial and viscous term magnitudes:

$$Re_e^f = \frac{\rho\frac{{v^f}^2}{h}}{\mu\frac{v^f}{h^2}} = \frac{\rho v^f h}{\mu}. \tag{20}$$

The fluid domain velocity magnitude v^f varies throughout the design domain and is not known when selecting $\overline{D}_1$. An estimation of the magnitude $\tilde{v}^f \approx v^f$ is thus needed to evaluate the elemental Reynolds number:

$$\widetilde{Re}_e^f \approx \frac{\rho\tilde{v}^f h}{\mu} \tag{21}$$

Generally, we estimate $\tilde{v}^f$ using the maximum velocity magnitude at the inlet or outlet. For low elemental Reynolds number, $\widetilde{Re}_e^f \leq 1$, viscous terms are dominant and Eq. (19) reduces to $\mu v^f/h^2 \approx \overline{D}_1 v^s$, such that we can compute the flow reduction as:

$$\frac{v^s}{v^f} \approx \frac{\mu}{h^2\overline{D}_1} \approx 10^{-q}. \tag{22}$$

Subsequently, we find a maximum penalization for the desired flow reduction:

$$\overline{D}_1 = 10^q\frac{\mu}{h^2}. \tag{23}$$

To summarize, we first used the fact that $\mathcal{O}^f\left(\boldsymbol{R}_{\mathbf{v}}\right) \approx \mathcal{O}^s\left(\boldsymbol{R}_{\mathbf{v}}\right)$ to find an expression for the ratio of velocity magnitudes v^s/v^f. Subsequently, $\overline{D}_1$ is defined to ensure that this ratio approximately takes a desired value, i.e., $v^s/v^f \approx 10^{-q}$. A similar method will be used to define all other penalization magnitudes.

For low elemental Reynolds numbers, $\widetilde{Re}_e^f \leq 1$, the definition of the maximum Darcy penalization is straightforward. However, for larger elemental Reynolds numbers, $\widetilde{Re}_e^f > 1$, the inertial term is dominant and Eq. (19) reduces to $\rho{v^f}^2/h \approx \overline{D}_1 v^s$, such that flow reduction is computed as:

$$\frac{v^s}{v^f} \approx \frac{\rho v^f}{h\overline{D}_1} \approx 10^{-q}, \tag{24}$$

which holds for:

$$\overline{D}_1 = 10^q\frac{\rho v^f}{h} \approx 10^q\frac{\rho\tilde{v}^f}{h} = 10^q\frac{\mu}{h^2}\widetilde{Re}_e^f. \tag{25}$$

The estimation of the velocity magnitude $\tilde{v}^f$ influences the selection of $\overline{D}_1$ in two ways: first in selecting whether inertial or viscous terms are dominant in $\widetilde{Re}_e^f$, and second when inertial terms are dominant in selecting the penalization $\overline{D}_1$. An inaccurate estimation of the velocity $\tilde{v}^f$ influences the flow reduction, as shown by Theulings et al. [14]. Therefore, in this work, we aim to construct a penalization that does not require an *a priori* estimation of the velocity.

2.3. The Darcy with Forchheimer approach

To circumvent the estimation of the velocity magnitude $\tilde{v}^f$, we add the Forchheimer penalization [10] to the momentum equation, resulting in the Darcy with Forchheimer (DF) approach. The Forchheimer penalization depends quadratically on the velocity and is introduced beside the Darcy penalization as:

$$\boldsymbol{R}_{\mathbf{v}}(\mathbf{v}, p) = -\rho\nabla\mathbf{v}\cdot\mathbf{v} - \nabla p + \nabla\cdot\left(\mu\left(\nabla\mathbf{v} + \nabla\mathbf{v}^\top\right)\right) \overbrace{-D_2(\alpha)\mathbf{v}}^{\text{Darcy penalization}} \underbrace{-F_2(\alpha)|\mathbf{v}|_2\mathbf{v}}_{\text{Forchheimer penalization}} = \mathbf{0}. \tag{26}$$

Both penalizations are set to zero $D_2(\alpha = 1) = F_2(\alpha = 1) = 0$ in the fluid domain and to their maximum value $D_2(\alpha = 0) = \overline{D}_2$, $F_2(\alpha = 0) = \overline{F}_2$ in the solid domain. To add the Forchheimer term to the order analysis performed in Section 2.2, we estimate its magnitude in the solid domain as:

$$\mathcal{O}^s\left(F_2(\alpha)\left|\mathbf{v}^h\right|_2\mathbf{v}^h\right) \approx \overline{F}_2\left(v^s\right)^2, \tag{27}$$

whereas its magnitude is set to zero in the fluid domain. Subsequently, we introduce the magnitude of the Forchheimer penalization to the right-hand side of Eq. (19):

$$\max\left(\rho\frac{{v^f}^2}{h}, \mu\frac{v^f}{h^2}\right) \approx \max\left(\overline{D}_2 v^s, \overline{F}_2 (v^s)^2\right). \tag{28}$$

We aim for the Forchheimer penalization to counteract inertial terms, as both scale quadratically with velocity, and for the Darcy penalization to counteract viscous terms, as both scale linearly with velocity. Neglecting the viscous ($Re_e^f \geq 1$) or inertial ($Re_e^f < 1$) terms, we find:

$$Re_e^f \geq 1 : \rho\frac{{v^f}^2}{h} \approx \overline{F}_2 (v^s)^2, \tag{29}$$

$$Re_e^f < 1 : \mu\frac{v^f}{h^2} \approx \overline{D}_2 v^s, \tag{30}$$

from which we derive the desired flow reduction and consequent maximum penalization magnitude as:

$$Re_e^f \geq 1 : \frac{v^s}{v^f} \approx \sqrt{\frac{\rho}{h\overline{F}_2}} \approx 10^{-q}, \qquad \overline{F}_2 = 10^{2q}\frac{\rho}{h}, \tag{31}$$

$$Re_e^f < 1 : \frac{v^s}{v^f} \approx \frac{\mu}{h^2\overline{D}_2} \approx 10^{-q}, \qquad \overline{D}_2 = 10^{q}\frac{\mu}{h^2}. \tag{32}$$

We find that the Forchheimer magnitude scales similarly to the Darcy magnitude in the D approach when inertial terms are dominant $\widetilde{Re}_e^f \geq 1$ in Eq. (25), but with a factor 10^{2q} instead of 10^q. Moreover, we emphasize that, contrary to the D approach, both terms in Eqs. (31) and (32) do not require an *a priori* velocity estimation.

2.4. The Darcy with filtered Forchheimer approach

The DF approach solves the problem of estimating $\tilde{v}^f$, but we find inconsistencies when performing numerical analysis in the assumptions made in the derivation of $\overline{F}_2$ and $\overline{D}_2$. We assumed that when inertial (resp. viscous) terms are dominant in the fluid, the Forchheimer (resp. Darcy) term is dominant in the solid. However, this assumption might not hold. To compare dominant terms, we define a solid domain elemental Reynolds number Re_e^s by inspecting the definition of Re_e^f. The fluid domain element Reynolds number in Eq. (20) was defined as the ratio between inertial and viscous term magnitudes, which is equivalent to dividing Eq. (29) by Eq. (30):

$$Re_e^f = \frac{\rho v^f h}{\mu} \approx \frac{\overline{F}_2 v^s}{\overline{D}_2}. \tag{33}$$

Subsequently, we define the solid domain elemental Reynolds number by substituting the maximum values for the Forchheimer/Darcy penalization in Eq. (33):

$$Re_e^s = \frac{\overline{F}_2 v^s}{\overline{D}_2} = 10^q\frac{\rho v^s h}{\mu}, \tag{34}$$

Using this definition, it should hold that $Re_e^f \approx Re_e^s$, i.e., the elemental Reynolds number should be continuous as it is of similar magnitude in neighboring solid and fluid domains. In the ideal case when $v^s = v^f 10^{-q}$ this holds as $Re_e^s = 10^q(\rho v^s h)/\mu = (\rho v^f h)/\mu$. However, it might happen that $Re_e^s \geq 1$, while $Re_e^f < 1$, or vice versa. This mainly occurs during the convergence of the state solution when we have not yet converged to a solution where $v^s/v^f = 10^{-q}$. When this occurs, Re_e^s and penalizations may abruptly change, resulting in unstable convergence behavior. Consequently, in our numerical analysis in Section 4, we find the DF approach to have less predictable solutions and a less predictable objective convexity. Moreover, in Appendix B jumps in the elemental Reynolds number are shown to lead to convergence problems of the forward solution. An alternative penalization approach, which ensures a more continuous elemental Reynolds number, is needed.

To solve this issue, we aim to define penalizations such that $Re_e^s = Re_e^f = \rho v^f h/\mu$, and Re_e^s should thus be dependent on the fluid domain velocities v^f. However, no field containing information on fluid domain velocities is present in the solid domain. To pull information from the fluid domain to the solid domain, we define the *filtered* velocity magnitude U by applying the PDE filter, as described for the design field by Lazarov and Sigmund [22], to the velocity magnitude:

$$-R^2\nabla^2 U + U = |\mathbf{v}|_2. \tag{35}$$

Information about the local flow velocity is distributed over a domain with a radius of N elements using $R = Nh/(2\sqrt{3})$, such that we may estimate $\mathcal{O}^s\left(U^h\right) \approx v^f$. Although the filtered velocity magnitude U will have a significant magnitude in the solid domain, which does not appropriately represent the physics, it can be used to appropriately penalize and decrease the actual magnitude of $\mathbf{v} = [u, v]^\top$ in the solid domain. The filtered velocity magnitude U thus exists in conjunction with the actual velocity and its magnitude

$|\mathbf{v}|_2$, i.e., no additional flow is introduced in the solid domain. We introduce a *filtered* Forchheimer penalization, resulting in the Darcy with filtered Forchheimer (DFF) approach:

$$\boldsymbol{R}_{\mathbf{v}}(\mathbf{v},p) = -\rho\nabla\mathbf{v}\cdot\mathbf{v} - \nabla p + \nabla\cdot\left(\mu\left(\nabla\mathbf{v}+\nabla\mathbf{v}^{\top}\right)\right) \overbrace{-D_3(\alpha)\mathbf{v}}^{\text{Darcy penalization}} \underbrace{-F_3(\alpha)U\mathbf{v}}_{\text{filtered Forchheimer penalization}} = \mathbf{0}. \tag{36}$$

The magnitude of the filtered Forchheimer penalization is estimated as $\mathcal{O}^s\left(F_3(\alpha)U^h\mathbf{v}^h\right) \approx \overline{F}_3 v^f v^s$, which is introduced in Eq. (19), to find:

$$\max\left(\rho\frac{{v^f}^2}{h}, \mu\frac{v^f}{h^2}\right) \approx \max\left(\overline{D}_3 v^s, \overline{F}_3 v^f v^s\right). \tag{37}$$

The Darcy penalization remains unchanged with respect to the DF approach and the maximum penalization $\overline{D}_3 = 10^q\mu/h^2$ found in Eq. (32) is used. When $Re_e^f \geq 1$ and inertial terms are dominant, we aim for the filtered Forchheimer penalization to inhibit the flow. We find $\rho\frac{{v^f}^2}{h} \approx \overline{F}_3 v^f v^s$, and a flow reduction with resulting maximum penalization:

$$\frac{v^s}{v^f} \approx \frac{\rho}{h\overline{F}_3} \approx 10^{-q}, \qquad \overline{F}_3 = 10^q\frac{\rho}{h}, \tag{38}$$

which is a factor 10^q lower than the maximum $\overline{F}_2$ for the DF approach in Eq. (31). Moreover, computing the solid domain elemental Reynolds number using the filtered Forchheimer penalization, we find:

$$Re_e^s = \frac{\overline{F}_3 v^f v^s}{\overline{D}_3 v^s} = \frac{\rho v^f h}{\mu} = Re_e^f. \tag{39}$$

Using the filtered Forchheimer penalization, we ensure a continuous elemental Reynolds number and appropriate penalization magnitudes for viscous and inertial terms.

2.5. Overview of penalization approaches

Three approaches for penalizing the flow in the solid domain are discussed in this paper: the Darcy, the Darcy with Forchheimer, and the Darcy with filtered Forchheimer approach, defined respectively as:

$$\text{D:} -\rho\nabla\mathbf{v}\cdot\mathbf{v} - \nabla p + \nabla\cdot\left(\mu\left(\nabla\mathbf{v}+\nabla\mathbf{v}^{\top}\right)\right) - D_1(\alpha)\mathbf{v} = \mathbf{0} \tag{40}$$

$$\text{DF:} -\rho\nabla\mathbf{v}\cdot\mathbf{v} - \nabla p + \nabla\cdot\left(\mu\left(\nabla\mathbf{v}+\nabla\mathbf{v}^{\top}\right)\right) - D_2(\alpha)\mathbf{v} - F_2(\alpha)|\mathbf{v}|_2\mathbf{v} = \mathbf{0}, \tag{41}$$

$$\text{DFF:} -\rho\nabla\mathbf{v}\cdot\mathbf{v} - \nabla p + \nabla\cdot\left(\mu\left(\nabla\mathbf{v}+\nabla\mathbf{v}^{\top}\right)\right) - D_3(\alpha)\mathbf{v} - F_3(\alpha)U\mathbf{v} = \mathbf{0}. \tag{42}$$

Subsequently, maximum penalizations are defined such that the flow reduction at the fluid/solid interface can be approximated as $v^s/v^f = 10^{-q}$. For the D approach, an appropriate penalization depends on an estimate of the fluid velocity magnitude and consequent elemental Reynolds number in Eq. (21). The maximum penalization values derived in previous sections can be found in Table 1.

Table 1
The derived appropriate settings for the maximum penalization in the solid domain at $\alpha = 0$ such that the flow reduction can be estimated as $v^s/v^f = 10^{-q}$.

	D: $\widetilde{Re}_e^f \leq 1$	D: $\widetilde{Re}_e^f > 1$	DF	DFF
Darcy	$\overline{D}_1 = 10^q\frac{\mu}{h^2}$	$\overline{D}_1 = 10^q\frac{\mu}{h^2}\widetilde{Re}_e^f$	$\overline{D}_2 = 10^q\frac{\mu}{h^2}$	$\overline{D}_3 = 10^q\frac{\mu}{h^2}$
Forchheimer	–	–	$\overline{F}_2 = 10^{2q}\frac{\rho}{h}$	$\overline{F}_3 = 10^q\frac{\rho}{h}$

2.6. Interpolation function and post-processing approach

So far, this section has mainly focused on the flow reduction at crisp fluid/solid interfaces. However, since gradient-based optimization with continuous design variables is used, we interpolate the penalization $D(\alpha)$ and $F(\alpha)$ for $0 \leq \alpha \leq 1$, and fluid/solid interfaces generally exhibit intermediate values of α. In this work, we use the interpolation function presented by Borrvall and Petersson [4] and shown in Fig. 2:

$$D(\alpha) = \overline{D}\frac{\hat{p}(1-\alpha)}{\hat{p}+\alpha}, \tag{43}$$

where the parameter $\hat{p}$ was originally introduced in a two-step continuation approach to control the level of gray in the optimized designs. The layout is first optimized using $\hat{p} = 0.01$ to make the response surface of the objective more convex and allow the optimizer to escape ill-performing local optima. Secondly, the resulting designs are further optimized using $\hat{p} = 0.1$ to obtain a discrete valued solution. In Section 4.2, the relation between the interpolation function and convexity of the pressure drop objective will be further investigated.

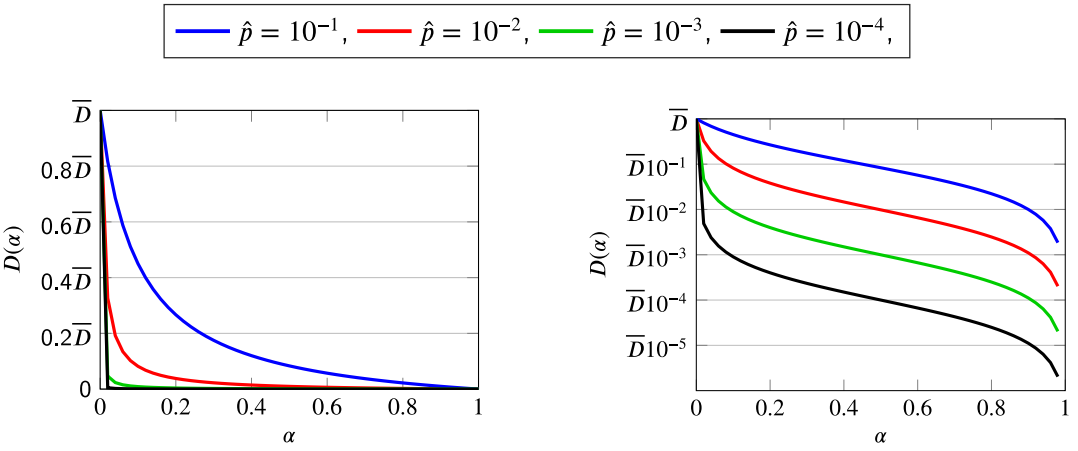

Fig. 2. The interpolation function presented in Eq. (43) in linear and logarithmic scales.

Our approach for finding appropriate interpolation functions is to examine a fluid/solid interface, where the solid domain in Fig. 1 is replaced by a porous domain with $\alpha \approx 0.5$. We note that [5] already interpret the interpolation as a function which decreases the penalization in the gray areas to improve the convexity of the objective response. However, using our prediction of the flow reduction, a more reliable derivation of the required parameter $\hat{p}$ can be obtained. We investigate the penalization achieved for these interface areas by observing that the interpolation lowers the magnitude of the penalization determined by 10^q in Table 1, and consequently increases the predicted flow. In all approaches, the Darcy penalization is interpolated by using $\hat{p} = 10^{-\hat{q}}$ in Eq. (43), as:

$$D(\alpha) = \overline{D}\frac{10^{-\hat{q}}(1-\alpha)}{10^{-\hat{q}}+\alpha}, \tag{44}$$

such that $D(\alpha = 0.5) \approx 10^{-\hat{q}}\overline{D}$, decreasing the Darcy penalization by $10^{-\hat{q}}$ as shown in the logarithmic plot in Fig. 2, resulting in more porous domain flow as $v^s/v^f = 10^{\hat{q}-q}$.

For the Forchheimer penalization, a different interpolation function is used for the DF and the DFF approach where we substitute $\hat{p} = 10^{-2\hat{q}}$ and $\hat{p} = 10^{-\hat{q}}$, respectively:

$$F_2(\alpha) = \overline{F}_2\frac{10^{-2\hat{q}}(1-\alpha)}{10^{-2\hat{q}}+\alpha}, \qquad F_3(\alpha) = \overline{F}_3\frac{10^{-\hat{q}}(1-\alpha)}{10^{-\hat{q}}+\alpha}, \tag{45}$$

such that at the fluid/solid interface $F_2(\alpha = 0.5) \approx 10^{-2\hat{q}}\overline{F}_2$ and $F_3(\alpha = 0.5) \approx 10^{-\hat{q}}\overline{F}_3$, decreasing the penalization by $10^{-2\hat{q}}$ and $10^{-\hat{q}}$, respectively. In Table 1, the penalizations for the DF and DFF approach scale respectively with 10^{2q} and 10^q, both resulting in a flow reduction of $v^s/v^f = 10^{-q}$. The lower parameter $\hat{p} = 10^{-2\hat{q}}$ for the DF approach is thus needed to ensure that the flow in the porous domain scales similarly for the DF and DFF approaches as $v^s/v^f = 10^{\hat{q}-q}$.

Using the predicted flow reduction in porous areas, we derive an improved threshold on α for the post-processing of optimized results. Common approaches for post-processing define the solid domain as the areas where $\alpha < \alpha_t = 0.5$. However, using our prediction of the flow reduction, we define the solid domain as the domain where a specific flow reduction is achieved and derive a specific value α_t dependent on both q and $\hat{q}$. For a specific flow reduction of 10^{-r}, we require an interpolated Darcy magnitude of $D(\alpha_t) = \overline{D}10^{r-q}$, and the solid domain is defined as those areas where:

$$\frac{10^{-\hat{q}}(1-\alpha)}{10^{-\hat{q}}+\alpha} > 10^{r-q}, \tag{46}$$

which can be used to threshold the design using the interpolation function itself, or be rewritten as a threshold for α in the solid domain:

$$\alpha_t < \frac{1-10^{r-q}}{1+10^{r-q+\hat{q}}}. \tag{47}$$

The same threshold for α_t is found using the interpolation function in Eq. (45) for the Forchheimer penalization in the DF approach. For the remainder of this work, we threshold the designs using $r = 1$ such that the solid domain is defined as those areas where $v^s/v^f < 0.1$.

3. Numerical implementation

For the analysis and optimization of the flow problems, we use [20]. Since the implementation is done by the multiphysics software, we take a birds-eye view of the model. However, it remains important to make informed choices of the settings within the software.

3.1. Discretization and optimization approach

Shape functions, stabilization approaches, and solution procedures have to be specified for the flow field, pressure field, and filtered flow field. All fields are discretized using the finite element method on the same quadrilateral mesh with square elements of size h. For the flow field we use quadratic while for the pressure field we use linear interpolation functions. The filtered velocity field is handled similarly to the velocity field with quadratic interpolation functions. Streamline diffusion [23,24] is used to stabilize the solution when convection is dominating the flow. In our changing topology, small islands or sharp corners may appear, therefore, to stabilize the solution around these features, additional diffusion is added by applying crosswind diffusion [23,25]. We note that streamline and crosswind diffusion slightly lower the accuracy of the flow solution, although not significantly in comparison to errors related to flow leakage. However, the use of these stabilization terms promote a smooth convergence of the flow solution.

Finally, the design is represented using a constant volume fraction α in each element in the mesh, and no filter is applied on the design variables. Furthermore, we use the Method of Moving Asymptotes (MMA) approach with an optimality tolerance of 10^{-3} and a constraint penalty factor of 10^2. The relatively low penalty factor allows for more design flexibility while satisfying the constraints within an acceptable tolerance. To compute sensitivities, the adjoint approach is used.

3.2. Stabilization of the state solution

To solve the state equations reliably for moderate Reynolds numbers, a pseudo time-stepping scheme is used [26], and a transient problem is solved until steady state is reached:

$$\boldsymbol{R}_v = -\rho\frac{\mathbf{v}^n - \mathbf{v}^{n-1}}{\Delta\tilde{t}} - \rho\nabla\mathbf{v}^n\cdot\mathbf{v}^n - \nabla p^n + \nabla\cdot\left(\mu\left(\nabla\mathbf{v}^n + \nabla\mathbf{v}^{n\top}\right)\right) - \boldsymbol{f}(\mathbf{v}^n) = \mathbf{0}, \tag{48}$$

where the superscript n denotes the iteration in the pseudo time-stepping scheme and $\boldsymbol{f}$ represents the selected penalization. Time steps are computed based on the local Courant–Friedrichs–Lewy (CFL) number as $\Delta\tilde{t} = CFL_{loc}\Delta\tilde{t}_r$, where the reference time step is defined as:

$$\Delta\tilde{t}_r = \frac{h}{|\mathbf{v}^n|_2}. \tag{49}$$

The local CFL number CFL_{loc} is determined by a PID regulator, and $|\mathbf{v}^n|_2$ the local velocity magnitude. This approach assumes that inertial terms are dominant on the element scale and are the limiting factor for a stable time step. However, using this approach, some solutions diverge in the forward solve during optimization. Upon close inspection, divergence happens for higher $q \geq 2$ and when an update in the design causes a new solid element to appear in the fluid domain. To speed up computations, we initialize the flow solution in the current design using the flow solution from the previous design. We found this may cause large non realistic flow speeds and consequently diverging flow solutions in the newly introduced solid elements.

We solve the stability issue by investigating the assumption of dominant inertia in penalized elements. In Section 2.2, we assumed that when inertia is dominant in the fluid domain, the penalization terms are dominant in the solid domain. As a consequence, the penalization term in should be dominant over the inertia terms in the solid domain. An appropriate time step in the solid domain should thus be dependent on the penalization magnitude.

To define an appropriate time step, we investigate the order of magnitude of the transient and the penalization term in the solid domain:

$$\mathcal{O}^s\left(\rho\frac{\mathbf{v}^n - \mathbf{v}^{n-1}}{\Delta\tilde{t}}\right) = \rho\frac{v^s}{\Delta\tilde{t}_f}, \qquad \mathcal{O}^s\left(\boldsymbol{f}\right) = |\boldsymbol{f}|_2 = f^s, \tag{50}$$

where we compute $v^s = |\mathbf{v}^n|_2$ at each time step, and define the magnitude of the penalization in the differing approaches as:

$$\text{D: } f^s = D_1(\alpha)v^s \tag{51}$$

$$\text{DF: } f^s = \left(D_2(\alpha) + F_2(\alpha)v^s\right)v^s, \tag{52}$$

$$\text{DFF: } f^s = \left(D_3(\alpha) + F_3(\alpha)U\right)v^s. \tag{53}$$

We use interpolated values $D(\alpha)$ and $F(\alpha)$ as instabilities may already occur in gray elements with relatively high penalization values. Subsequently, we assume the penalization is dominant and limits the maximum time step $(\rho v^s)/\Delta\tilde{t}_f = f^s$:

$$\text{D: } \Delta\tilde{t}_f = \frac{\rho}{D_1(\alpha)} \tag{54}$$

$$\text{DF: } \Delta\tilde{t}_f = \frac{\rho}{D_2(\alpha) + F_2(\alpha)v^s}, \tag{55}$$

$$\text{DFF: } \Delta\tilde{t}_f = \frac{\rho}{D_3(\alpha) + F_3(\alpha)U}. \tag{56}$$

In the fluid domain where $\alpha = 1$ and $\boldsymbol{f} = \mathbf{0}$, the inertial term remains dominant. Since the time step is computed per element and inversely proportional to either the inertia or penalization term, we use the smallest computed time step in our solution procedure.

$$\Delta\tilde{t} = CFL_{loc}\min\left(\Delta\tilde{t}_r, \Delta\tilde{t}_f\right). \tag{57}$$

To regularize the time step and speed up the computation the local CFL number is included in the time step definition.

We note that computational time is generally reduced when a direct steady-state solver is used instead of the pseudo time-stepping scheme. However, when Reynolds numbers increase, the presented pseudo time-stepping approach is often necessary for the state-solution to converge. Pseudo time-stepping performs more gradual updates of the flow and pressure fields, and generally needs more iterations to converge. This results in a larger computational cost, but a more smooth and reliable convergence behavior.

4. Model investigation

In Section 2, we described three penalization approaches that should lead to a flow reduction of $v^s/v^f = 10^{-q}$. In Section 4.1, we verify the predicted flow reduction. We expect the D approach to be less predictable due to the estimation of the fluid domain velocity magnitude and the DF and DFF approaches to achieve a more predictable flow reduction. In Section 4.2, we examine the convergence behavior of the optimization by investigating the convexity of the objective function, here chosen as the pressure drop.

4.1. Model accuracy and flow leakage

To investigate the flow leakage, we use the setup in Fig. 3 and the geometry and material parameters in Table 2. Different inlet Reynolds numbers Re_{in} are investigated and we define the fluid density as:

$$\rho = \frac{Re_{in}\mu}{\overline{v}L}, \tag{58}$$

where $\overline{v}$ is the maximum inlet velocity and L the inlet diameter. For the D approach, we estimate the fluid domain flow speed using the maximum inlet velocity $\overline{v}$. For the DFF approach, we filter the velocity over $N = 10$ elements, i.e., $R = Nh/(2\sqrt{3})$, based on the findings from Appendix A on the effect of the filter radius on flow leakage. The choice of $N = 10$ is based on the maximum filter radius for which overpenalization does not occur.

To check the predictability of the flow leakage, we place solid obstacles with $\alpha = 0$ either in the center (Ω_i^c) or towards the edge (Ω_i^e) of all $i \in \{1 : 6\}$ channels. The design is constructed such that different elemental Reynolds numbers occur naturally in different parts of the domain. In Channel 6, low flow velocities lead to low elemental Reynolds numbers, while in Channel 1, larger flow velocities lead to relatively high elemental Reynolds numbers. Additionally, flow speeds and elemental Reynolds numbers near the channel walls are significantly lower than in the center of the channels. A unique estimation $\tilde{v}^f$ and thus $\widetilde{Re}_e^f$ for the penalization in the D approach does not exist as the velocity varies throughout the domain, a situation that often occurs during topology optimization.

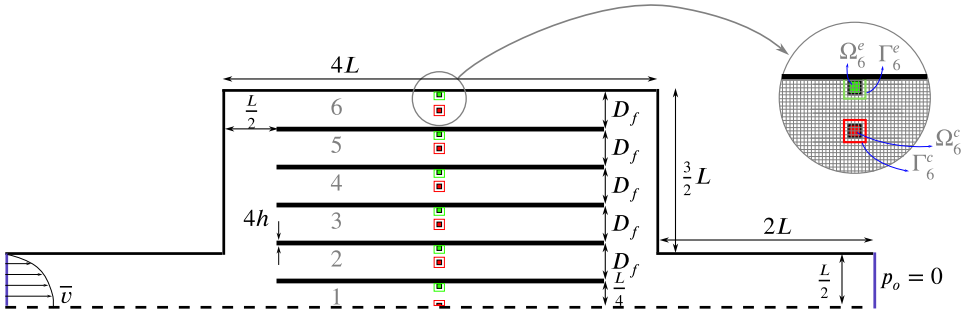

Fig. 3. The setup to measure the accuracy of the predicted flow leakage. The design is symmetric over the dashed boundary. In Channel 1 to 6, obstacles with volume fraction $\alpha = 0$ are placed. We either add the green obstacles Ω_i^e at the edge or the red obstacles Ω_i^c in the center of the channels. Obstacles consist of a four by four element domain. To measure the flow leakage relative to the local flow magnitude, we define fluid edges Γ_i^e and Γ_i^c as the edges one element away from Ω_i^e and Ω_i^c, respectively. (For interpretation of the references to color in this figure legend, the reader is referred to the web version of this article.)

Table 2
The parameters used to verify the predicted flow leakage using the setup in Fig. 3.

L	D_f	h	μ	$\overline{v}$	$\tilde{v}^f$	N
1 [m]	$\frac{7L}{20}$	$\frac{L}{80}$	1 [Pa s]	10 [m s^{-1}]	$\overline{v}$	10

We compute the flow leakage by comparing the average flow magnitude within obstacles Ω_i^e or Ω_i^c to the average flow speed on Γ_i^e or Γ_i^c, the fluid edges located one element away from the obstacles. Superscripts c and e denote center and edge obstacles, respectively. To average the flow speeds, we use the surface area for the obstacles A_Ω, and length of the center or edge boundaries L_{Γ^c} or L_{Γ^e}, respectively. The flow leakage is computed as:

$$\epsilon_i^{\mathrm{e}} = \frac{v^s}{v^f} \approx \frac{\int_{\Omega_i^{\mathrm{e}}} |\mathbf{v}|_2 d\Omega}{\int_{\Gamma_i^{\mathrm{e}}} |\mathbf{v}|_2 d\Gamma} \frac{L_{\Gamma^e}}{A_\Omega}, \qquad \epsilon_i^{\mathrm{c}} = \frac{v^s}{v^f} \approx \frac{\int_{\Omega_i^{\mathrm{c}}} |\mathbf{v}|_2 d\Omega}{\int_{\Gamma_i^{\mathrm{c}}} |\mathbf{v}|_2 d\Gamma} \frac{L_{\Gamma^c}}{A_\Omega} \tag{59}$$

After computing the flow leakage from our solution, we check it against our prediction of $v^s/v^f = 10^{-q}$. The order of the flow reduction $\tilde{q}$ in the ith channel can be computed when solving with a different $q \in 0, 1, 2, 3$, as:

$$\tilde{q}_{q,i}^e = -\log_{10}\left(\epsilon_i^e\right), \qquad \tilde{q}_{q,i}^c = -\log_{10}\left(\epsilon_i^c\right), \tag{60}$$

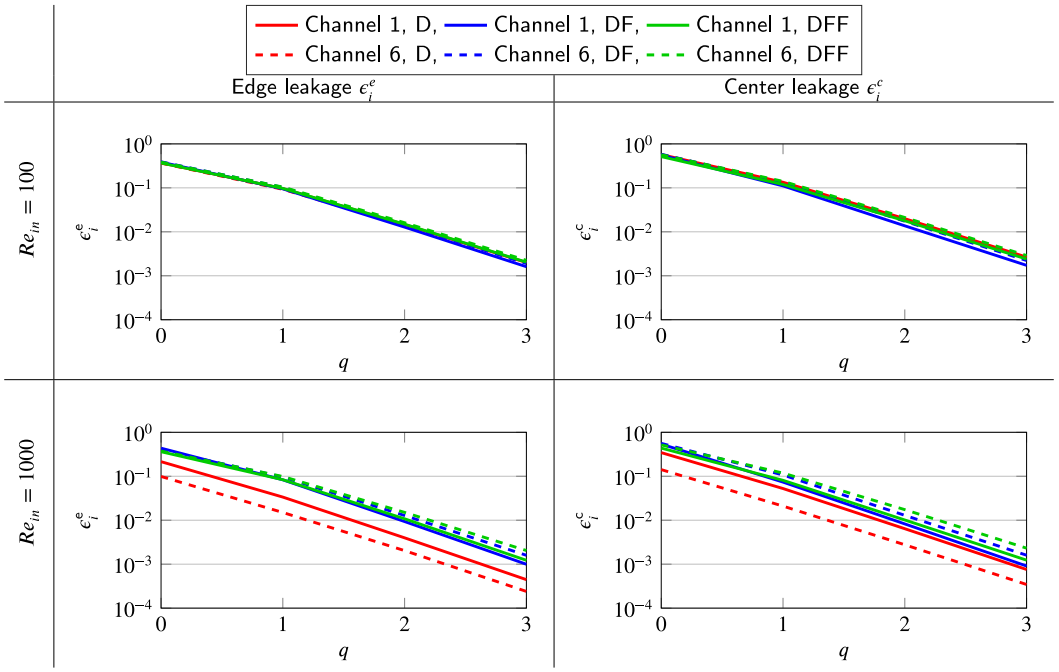

Fig. 4. Trend in the flow leakage for increasing q in the problem in Fig. 3 with parameters in Table 2. Errors for Channel 1 and 6 are shown as these channels present the highest and lowest flow magnitudes. Both the DF and DFF approaches predict errors well as 10^{-q}. The D approach predicts errors well for low but not for high Reynolds numbers.

Table 3
The error in flow reduction for the center obstacles (ξ^c), edge obstacles (ξ^e) for moderate ($Re_{in} = 100$, $Re_e^f \leq 1$) and relatively high ($Re_{in} = 1000$, $Re_e^f > 1$) Reynolds numbers. Examining the errors, the DF approach is found to be the most accurate followed by the DFF and D approaches.

	ξ^e, $Re = 100$	ξ^e, $Re = 1000$	ξ^c, $Re = 100$	ξ^c, $Re = 1000$
D	0.159	0.627	0.280	0.462
DF	0.142	0.086	0.217	0.102
DFF	0.188	0.137	0.299	0.176

where subscript q denotes the user-defined parameter for the solution. The measured magnitude of the flow reduction is subsequently used to compute a mean error with respect to our prediction:

$$\xi^e = \frac{\sum_{q=1}^{3}\sum_{i=1}^{6}\left|q - \tilde{q}_{q,i}^e\right|_2}{18}, \qquad \xi^c = \frac{\sum_{q=1}^{3}\sum_{i=1}^{6}\left|q - \tilde{q}_{q,i}^c\right|_2}{18}. \tag{61}$$

We do not include results for $q < 1$ in the verification as the flow reduction associated to such values is too low to be accurate and all approaches show similar results. The analysis will be performed for moderate and relatively high inlet Reynolds numbers $Re = 100$ and $Re = 1000$ such that low ($Re_f^e < 1$) and high ($Re_f^e > 1$) elemental Reynolds numbers are present.

In Fig. 4, the measured flow leakage for varying q can be found. We present only errors in Channels 1 and 6 as in these channels, the highest and lowest flow magnitudes and elemental Reynolds numbers are found, as shown in Fig. 5. The first observation is that for $Re = 100$, the D approach is in good agreement with the prediction, while for $Re = 1000$, it overpenalizes flow leading to an increased flow reduction. This is caused by an erroneous estimation $\tilde{v}^f$ of the velocity magnitude. For $Re = 100$, the approximate elemental Reynolds number is low $\widetilde{Re}_e^f = 1.25$ and the estimation of $\tilde{v}^f$ does not significantly influence the penalization. For $Re = 1000$, the approximate elemental Reynolds number is larger, $\widetilde{Re}_e^f = 12.5$, and the magnitude of the penalization is largely dependent on the estimation of $\tilde{v}^f$. The estimation of the flow velocity is only valid in the center of Channel 1 where $\widetilde{Re}_e^f \approx Re_e^f$. For all other obstacles, the flow velocity is overestimated leading to excessive flow reduction.

As reported in Table 3 by the errors in prediction ξ, both the DF and DFF approaches produce more predictable errors, whereas errors in the D approach spike for $Re = 1000$. In all cases, the DF approach is found to be the most accurate. However, the DF approach shows convergence problems, even with the stabilization procedure in Section 3.2 and generally takes more iterations to converge. For high Reynolds numbers, the D approach does not predict flow leakage accurately which will cause problems for the optimization procedure as examined in Sections 4.2 and 5.

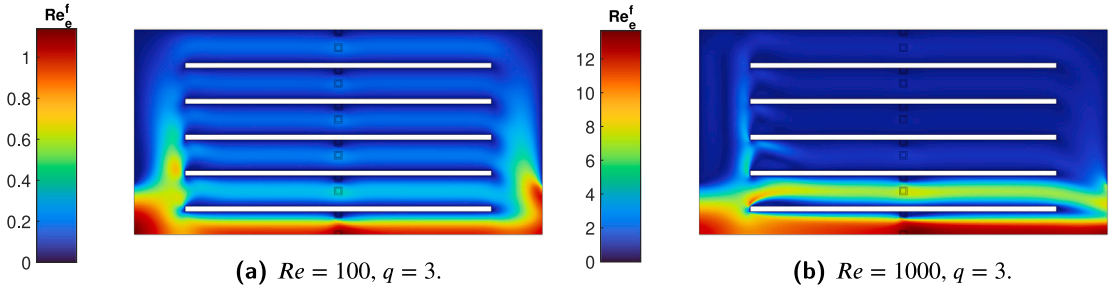

(a) $Re = 100, q = 3.$ **(b)** $Re = 1000, q = 3.$

Fig. 5. Elemental Reynolds number Re_e^f, computed using the D approach. Only edge obstacles Ω_i^e are introduced. Using $\tilde{v}^f = \overline{v}$, we obtain an approximate elemental Reynolds number of $\widetilde{Re}_e^f = 1.25$ ($Re = 100$) and $\widetilde{Re}_e^f = 12.5$ ($Re = 1000$).

4.2. Objective convexity and continuation approach

To use the D, DF, or DFF approach for TO effectively, a continuation strategy is derived by investigating the effect of design changes on the objective. In particular, we study how the magnitude of the flow reduction and the shape of the interpolation function for the Darcy and the Forchheimer penalization affect an objective function, here chosen as the pressure drop:

$$g_p = \int_{\Gamma_o} p d\Gamma - \int_{\Gamma_i} p d\Gamma, \tag{62}$$

where Γ_o and Γ_i are the flow outlets and inlets, respectively. To examine the interaction between objective and penalization, we use the problems described in Fig. 6 with parameters in Table 4, and a Reynolds-dependent density:

$$\rho = \frac{Re_{in}\mu}{\overline{v}L_c}, \tag{63}$$

where L_c is the inlet diameter. To study the convexity of the objective response, we perform a similar analysis as [17], who inspect the monotonicity of the objective response for fluid structure interaction problems. We impose a change in design variable from solid, $\alpha = 0$, through gray, $\alpha \approx 0.5$, to fluid, $\alpha = 1$, for certain areas of the design. A convex response presents lower values for gray than for crisp designs, while a concave response takes lower values for crisp than for gray designs. Therefore, a convex response leads to designs that more freely change than for a concave response. Based on this information, a continuation approach can be derived to allow for large design updates in the early optimization stages and to ensure a crisp 0/1 design in later stages.

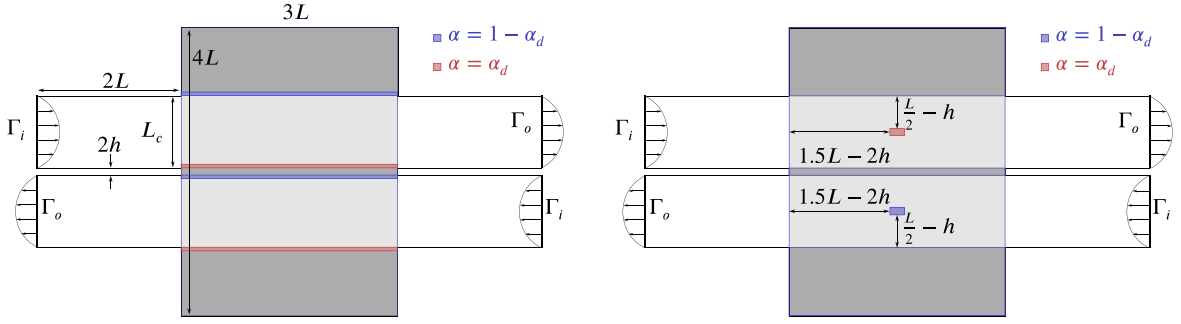

(a) The viscous dominated design change. (b) The inertia dominated design change.

Fig. 6. The two-channel problems used to investigate the convexity of the objective. On the inlets Γ_i, a parabolic inflow is applied and on the outlets Γ_o, a parabolic outflow is applied. Both parabolic in- and outflows have maximum velocity $\overline{v}$. In the red and blue areas, the design is changed. While the light gray is fluid ($\alpha = 1$) and the dark gray solid ($\alpha = 0$), the red and blue areas are changed through gray ($\alpha \approx 0.5$) from solid to fluid or vice versa. (For interpretation of the references to color in this figure legend, the reader is referred to the web version of this article.)

Table 4
Parameters for the analysis of the objective convexity for the problem in Fig. 6.

L	L_c	h	μ	$\overline{v}$	$\tilde{v}^f$
1 [m]	L	$\frac{L}{20}$	1 [Pa s]	1 [m s^{-1}]	$\overline{v}$

Two design changes, regulated by parameter $0 \geq \alpha_d \geq 1$, are examined as shown in Fig. 6. In Fig. 6(a), the channel walls are perturbed over one element to examine viscous dominated design changes. For $\alpha_d = 1$, the upper channel is straight while the lower channel is curved, and vice versa for $\alpha_d = 0$. In Fig. 6(b), a four-by-two-element-island is introduced in the center of the channel to examine inertia dominated design changes. For $\alpha_d = 1$, an island is present only in the top channel, and for $\alpha_d = 0$, only in the

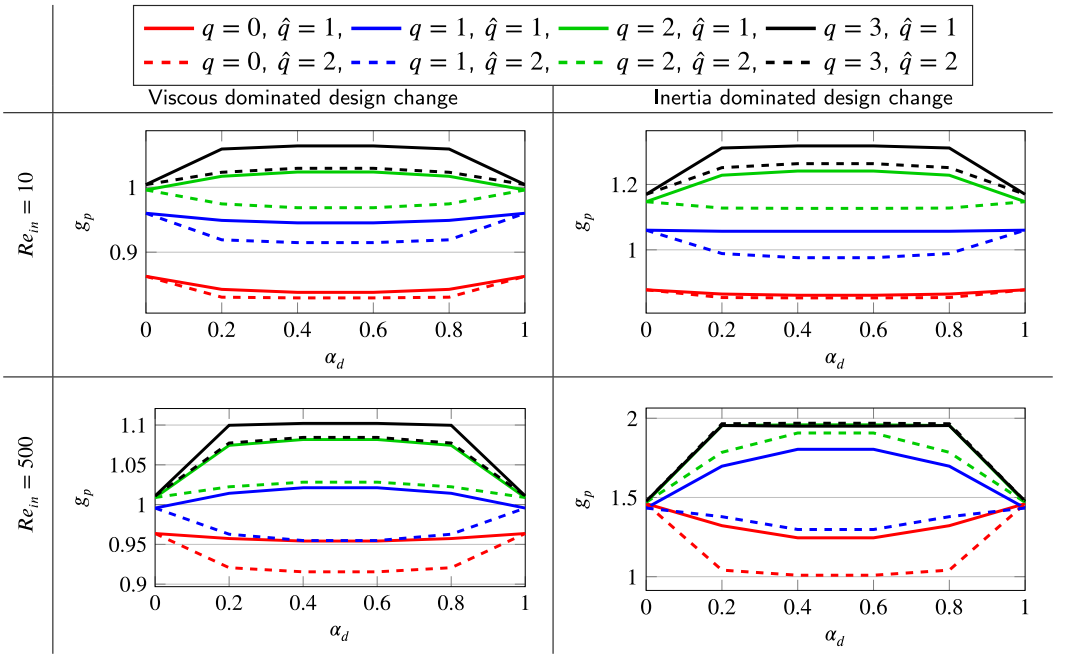

Fig. 7. Convexity of the pressure drop for the DFF approach using a viscosity dominated (Fig. 6(a)) or an inertia dominated design change (Fig. 6(b)) at Reynolds number $Re_{in} = 10{,}500$.

bottom channel. The design changes are symmetric to ensure the overall volume fraction in the design domain remains constant, as most optimization procedures involve an active volume fraction constraint. Additionally, as the designs for $\alpha_d = 0$ and $\alpha_d = 1$ are the same when mirrored over the center wall, we find the same objective values for these designs, which allow us to visually observe whether the response is concave or convex.

We present the pressure drop objective g_p for different values of α_d in the two designs defined by Figs. 6(a) and 6(b) using either $Re_{in} = 10$ or $Re_{in} = 500$ for, respectively, the DFF , DF, and D approach in Figs. 7, 8, and 11. The penalization in the gray areas is lowered using the penalization interpolation approach described in Section 2.6 using $\hat{q} \in \{1, 2\}$ and the maximum penalization magnitude is defined by $q \in \{0, 1, 2, 3\}$, which should lead to a flow reduction at the gray/fluid interface of $v^s/v^f = 10^{\hat{q}-q}$.

First, we analyze the convexity of the objective using the DFF approach in Fig. 7 and find a clear switch between convex and concave behavior. When the predicted flow reduction is $v^s/v^f = 10^{-q+\hat{q}} > 1$ (q< $\hat{q}$), the response is convex, when it is $v^s/v^f < 1$ (q> $\hat{q}$), the response is concave, and when it is exactly $v^s/v^f = 1$ ($q = \hat{q}$), the response differs between the sub-figures and is undetermined. We note that for a predicted $v^s/v^f \geq 1$, the penalization is not active and we measure $v^s/v^f \approx 1$. This behavior can be explained by the constant fluid volume associated to the design changes in Fig. 6. When the average volume fraction remains constant and gray areas emerge in the design, two scenarios may occur. If the penalization in the gray areas is low enough such that they can be seen as a fluid domain. The total "fluid" domain is increased, which is generally associated with less pressure drop. If the penalization is high enough such that the gray areas can be seen as a solid domain. The "solid" domain is increased which generally leads to an increase in pressure drop.

Secondly, we analyze the convexity of the objective using the DF approach in Fig. 8. We emphasize that following Section 2.6, a steeper interpolation is used for the Forchheimer than for the Darcy penalization. The DF approach does not present a consistent behavior as the DFF approach. For $Re_{in} = 10$, we find convex behavior for $q < \hat{q}$ and concave for $q > \hat{q}$, the same as the DFF approach. The response is thus convex for lower q and concave for higher q. However, for $Re_{in} = 500$ in the viscous dominated design change, we find different behavior. The response is concave for $q = 0$, convex for $q = 1$, and concave again for $q = 2$ and $q = 3$.

The difference in behavior between DF and DFF approaches can be understood from the flow profiles in Figs. 9(a) and 9(b). For $q = 0$, larger flow leakage through the center wall is observed for the DF approach compared to the DFF approach. Subsequently, the leakage causes the flow path to curve resulting in more pressure drop for the DF approach. Consequently, when gray elements are introduced $0 < \alpha_d < 1$ at the center wall, the resulting penalization lowers results in more flow leaking through the wall. This further deteriorates the objective, causing the DF response to be concave. However, for $q = 1$, the flow profile for the DF approach is similar to the profile for the DFF approach, and the response becomes convex.

To explain why the DF approach does not reproduce a flow solution similar to the DFF approach for $q = 0$, we further examine the DFF flow solution. In Section 2.4, we predicted that a difference in elemental Reynolds numbers in the solid and fluid domains may cause an abrupt change in penalization in the DF approach. In Fig. 10, the elemental Reynolds numbers are shown for the solution using $q = 0$ and $\alpha_d = 0$. The solid domain elemental Reynolds numbers are computed following Eq. (34) for the DF approach in Fig. 10(a), and using Eq. (39) for the DFF approach in Fig. 10(b). In both figures, the elemental Reynolds numbers are computed using

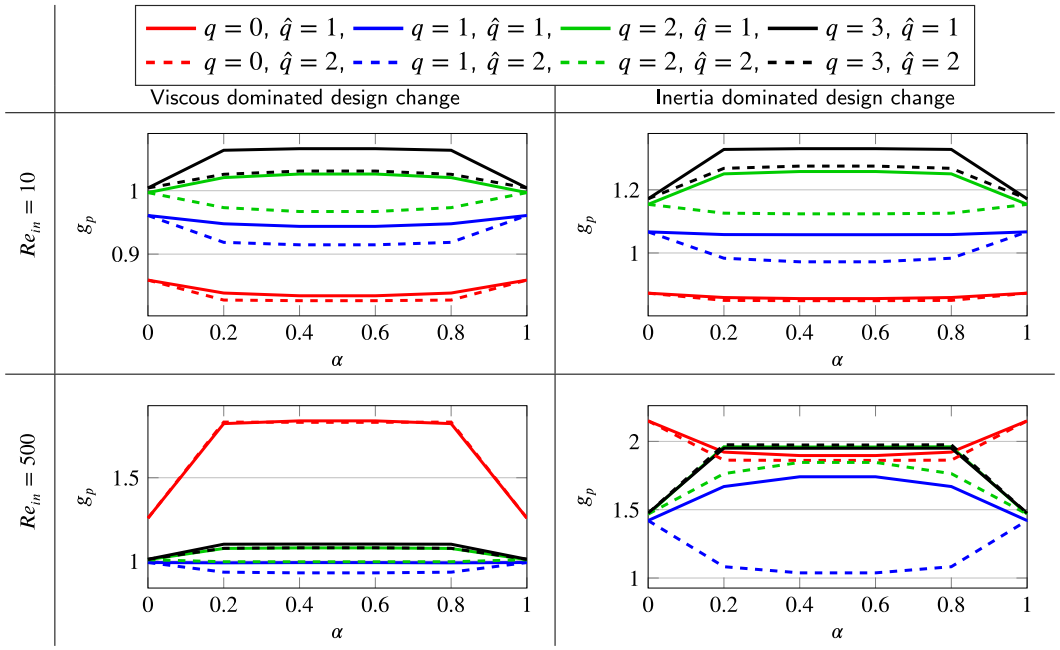

Fig. 8. Convexity of the pressure drop for the DF approach using a viscosity dominated (Fig. 6(a)) or an inertia dominated design change (Fig. 6(b)) at Reynolds number $Re_{in} = 10{,}500$.

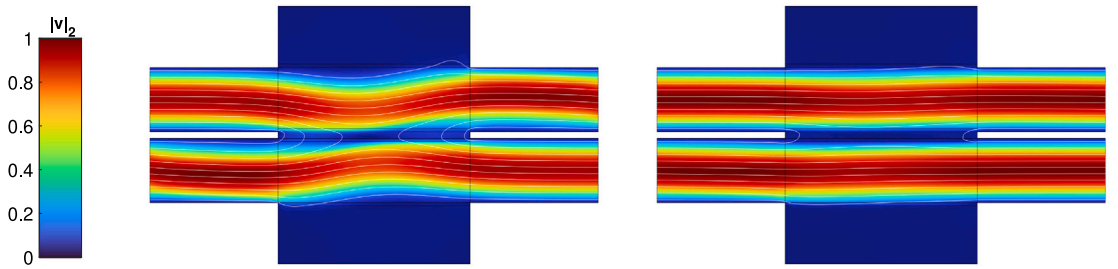

(a) DF flow profile (b) DFF flow profile

Fig. 9. Flow profiles for viscous dominated design change (Fig. 6(a)) for $q = 0$, $\hat{q} = 1$, $\alpha_d = 0$, and at $Re_{in} = 500$.

the DFF flow solution. The DFF elemental Reynolds numbers in Fig. 10(b) are of the same order of magnitude in the solid wall and in the channels. However, the DF elemental Reynolds numbers in Fig. 10(a) are at least one order of magnitude lower in the solid wall than in the channels. Moreover, in the solid domain the elemental Reynolds numbers are smaller than 1, $Re_e^s < 1$, while in the fluid domain, they are larger than one, $Re_e^f > 1$. In the solid domain, the Darcy penalization, which should inhibit viscous forces, is dominant, while in the fluid, inertial forces are dominant. For this reason, the flow solution found using the DFF approach cannot be obtained using the DF approach.

It is important to note that the DF approach is not less accurate nor that the flow leakage is less predictable. The examined results are computed for $q = 0$, which results in less predictable flow leakage for all approaches. Additionally, due to the curved flow path through the center wall in the DF flow solution in Fig. 9(a), flow speeds close to the wall (v^f) are higher resulting in a similar flow leakage (v^s/v^f) for both approaches. In fact, these results illustrate that the response computed using the DF approach is less predictable than the one computed with the DFF approach.

Finally, we examine the convexity of the pressure drop for the D approach in Fig. 11. Generally, the results are similar to those using the DFF approach, i.e., the response is convex for $q < \hat{q}$ and concave for $q > \hat{q}$. However, for $Re_{in} = 500$, $q = 0$, $\hat{q} = 1$ in the viscous dominated change and for $Re_{in} = 500$, $q = 1$, $\hat{q} = 2$ in the inertia dominated change, the response is neither completely concave or convex. This results from the estimation of the flow velocity, which leads to an elemental Reynolds number $\widetilde{Re}_e^f > 1$ and consequently to an overestimation of the required penalization in those areas where $Re_e^f < 1$. As we will show in Section 5, overpenalization can make the responses concave and leads to convergence to inferior local optima.

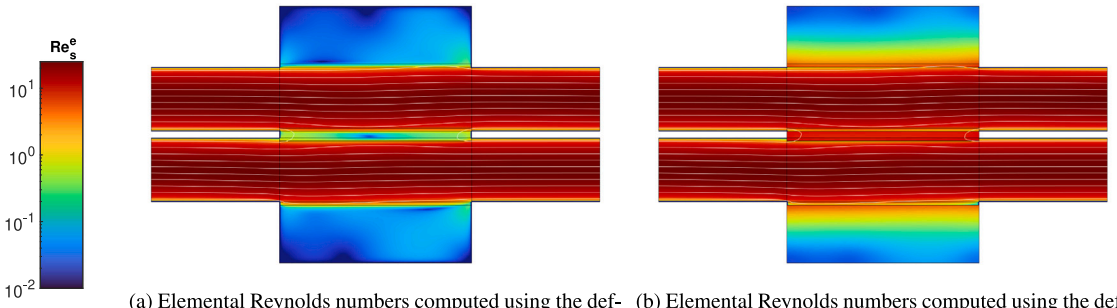

(a) Elemental Reynolds numbers computed using the definition for the DF approach ($Re_s^e = 10^{q\frac{\rho|\mathbf{v}|_2 h}{\mu}}$) in the solid domain.

(b) Elemental Reynolds numbers computed using the definition for the DFF approach ($Re_s^e = \frac{\rho U h}{\mu}$) in the solid domain.

Fig. 10. Elemental Reynolds numbers for the viscous design change (Fig. 6(a)) for $q = 0$, $\hat{q} = 1$, $\alpha_d = 0$, and $Re_{in} = 500$. All elemental Reynolds numbers are computed using the DFF flow solution in Fig. 9(b).

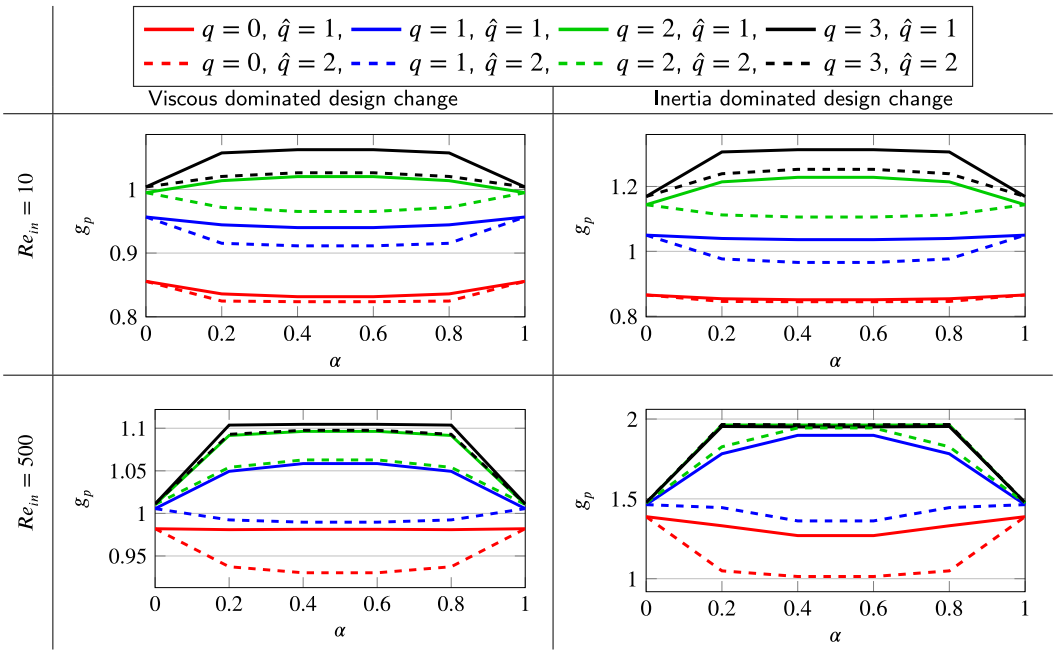

Fig. 11. Convexity of the pressure drop for the D approach using a viscosity dominated (Fig. 6(a)) or an inertia dominated design change (Fig. 6(b)) at Reynolds number $Re_{in} = 10{,}500$.

Using the results in this section, we create an informed continuation approach for optimization. In the initial stage of optimization, we are interested in the flexibility of the design while the accuracy is less important. In the later stage of optimization, we want to guide the design to a solid/fluid 0/1 solution which accurately describes the flow and thus the objective and constraint functions. We therefore use a continuation on q and optimize using low q in the initial stage and high q in the later stages. Another approach to add more convexity in the response is to use larger $\hat{q}$, as seen in Figs. 7, 8, and 11. However, in the authors' experience, adding a steeper slope to the interpolation function using $\hat{q} > 2$ generally deteriorates the convergence of the optimization procedure.

5. Topology optimization

In this section, we compare the penalization approaches using optimization examples. Section 5.1 focuses on the ability of the approaches to escape ill-performing local optima. In Section 5.2.1, we investigate the relation between design convergence and continuation, and show the limitations of the D approach under varying estimations of velocity magnitude $\tilde{v}^f$.

Beside accuracy and convexity, another important property is the stability of an approach. Stability with respect to the convergence of the flow solution, and with respect to the convergence of the optimization process. In our experience with the DF approach, design updates were often larger and less stable. Moreover, the solution procedure for the flow and pressure fields suffers from convergence issues, even using the stabilization approach described in Section 3.2. We found that the initial flow conditions

were more important for the flow/pressure fields to converge in the DF approach than in the D or DFF approaches. Using the D and the DFF approach, we could use the flow/pressure solution of the previous design as initial solution for the current design, resulting in much lower computational cost. Using the DF approach, we were often forced to reinitialize the flow/pressure fields resulting in large computational efforts. In Appendix B, we further investigate instabilities in the DF approach. Although the DFF approach is less predictable with respect to flow leakage than the DF approach, it is preferred for its stability. For the remainder of this chapter we do not consider the DF approach.

5.1. Dealing with ill-performing local optima

To examine the ability of the D and DFF approaches to escape inferior local optima, we use the problem introduced for the convexity analysis in Fig. 6. The parameters are provided in Table 5 for $Re_{in} = 500$ using the Reynolds dependent density defined in Eq. (63). The design domain is limited to the gray center areas and the inlet/outlet channels remain unchanged during the optimization. We expect optimized designs to consist of two straight channels with a parabolic flow profile. Using an inlet Reynolds number $Re_{in} = 500$, we expect the elemental Reynolds number Re^e_f to be larger than one in the center of the parabolic flow, and lower than one towards the channel walls.

Table 5
Parameters for the optimization of the problem in Fig. 6.

L	h	μ	$\bar{v}$	$\bar{v}^f$	N_i	q_{min}	q_{max}	Δq	$\hat{q}$	V_f
1 [m]	$\frac{L}{20}$	1 [m s]	1 [m s^{-1}]	$\bar{v}$	50	0	3	1	1, 2	$2L_c/4L$

In Section 4.2 we defined a general continuation approach which starts the optimization using a low q and ends using a high q. Specifically, we partition the optimization procedure into four stages of maximum $N_i = 50$ design iterations. Each part is terminated after the $N_i = 50$ iterations or when the largest change in a single design variable is less than 10^{-3}. We start the optimization using $q = q_{min} = 0$, and increase q after each stage by $\Delta q = 1$ until $q_{max} = 3$.

To examine the different approaches, we use a problem with a predictable optimum, i.e., two straight channels. This design would use $2L_c/4L$ of the design space and we set a volume constraint to:

$$g_v(\boldsymbol{\alpha}) = \frac{\sum_{i=1}^{N_\alpha} \alpha_i}{N_\alpha} - V_f \leq 0, \tag{64}$$

where we have N_α design variables α_i in the design domain Ω_d and $V_f = 2L_c/4L$. Two different inlet diameters and consequent volume constraints will be considered, $L_c = L$ and $L_c = L/2$. We normalize the pressure drop objective in Eq. (62) with the pressure drop associated to the two straight channel design, i.e., $g_{p0} = 112\mu\bar{v}L/L_c$.

Another important choice is the initial design $\alpha = \alpha_0 \in \Omega_d$. We use two approaches and either start with a fully fluid ($\alpha_0 = 1$) or gray ($\alpha_0 = V_f$) design. Starting from a fully fluid design, largely violating the volume constraint, leads to large design updates that tend to deteriorate the convergence of the forward problem. We found this effect to be worsened by increasing $\hat{q}$. A gray design initially inhibits the flow, decreasing the inertia effects, and favoring convergence towards designs with reduced viscous energy dissipation.

Optimal designs, raw (g^*_p), and post-processed ($g^*_{p,ref}$) objective values for the problem using $L_c = L$ are shown in Fig. 12, convergence history can be found in Fig. 13. It is noticeable that using $\hat{q} = 1$ inferior local optima with curved channels are found. For the D approach, both initial designs lead to the inferior optimum, while for the DFF approach, the inferior optimum is only found using $\alpha_0 = 1$ and the superior straight channel optimum is found using $\alpha_0 = V_f$. Increasing $\hat{q}$ to 2 improves the convexity of the objective response and allows the optimizer to escape the local optimum.

In the convergence history in Fig. 13, we find an increased convergence instability caused by using $\hat{q} = 2$ and $\alpha_0 = 1$. The objective of both the D and DFF approach show a large increase at iteration 4 caused by large design changes. When initializing using $\alpha_0 = 1$, the design violates the volume constraint resulting in relatively large design changes and objective fluctuations. Moreover, a spike in objective for the DFF approach using $\hat{q} = 2$ and $\alpha_0 = 1$ is observed at iteration 35. The volume fraction in the center wall, and the associated penalization, become too low, and flow leaks through the wall. As the volume fraction in the center wall, and consequently the penalization, is increased, the flow profile and objective stabilize. It should be noted that the DFF approach using $\hat{q} = 1$ and $\alpha_0 = V_f$ requires relatively few optimization iterations, see Fig. 13, and generates the desired topology quickly. Later increase in q do not lead to topology changes but help improve the accuracy of state solution.

Although improved design convergence is found for the D approach when using a more convex interpolation function with $\hat{q} = 2$, this cannot be generalized to other optimization problems. The same problem is investigated but with an inlet diameter $L_c = L/2$, a maximum volume fraction $V_f = 2L_c/4L$, and an estimated elemental Reynolds number $\widetilde{Re}^f_e = 50$. Resulting designs, raw (g^*_p), and post-processed ($g^*_{p,ref}$) objective values are given in Fig. 14, convergence history in Fig. 15. For this slight variation of the problem, the D approach converges to significantly different and inferior optima. The larger $\widetilde{Re}^f_e = 50$ results in a large maximum Darcy penalization $\overline{D}_1$. As predicted in Section 4.2, the penalization is overestimated for the straight channel optimum which is dominated by viscous effects. Consequently, the objective response becomes concave and the optimization process converges to an inferior local optimum dominated by inertial effects. Moreover, the D approach designs do not converge to fully solid/fluid designs and present larger gray areas which lower the accuracy of the raw objective values with respect to the post-processed ones, as shown by the large errors $Err_g = (g^*_{p,ref} - g^*_p)/g^*_{p,ref}$ in Fig. 14.

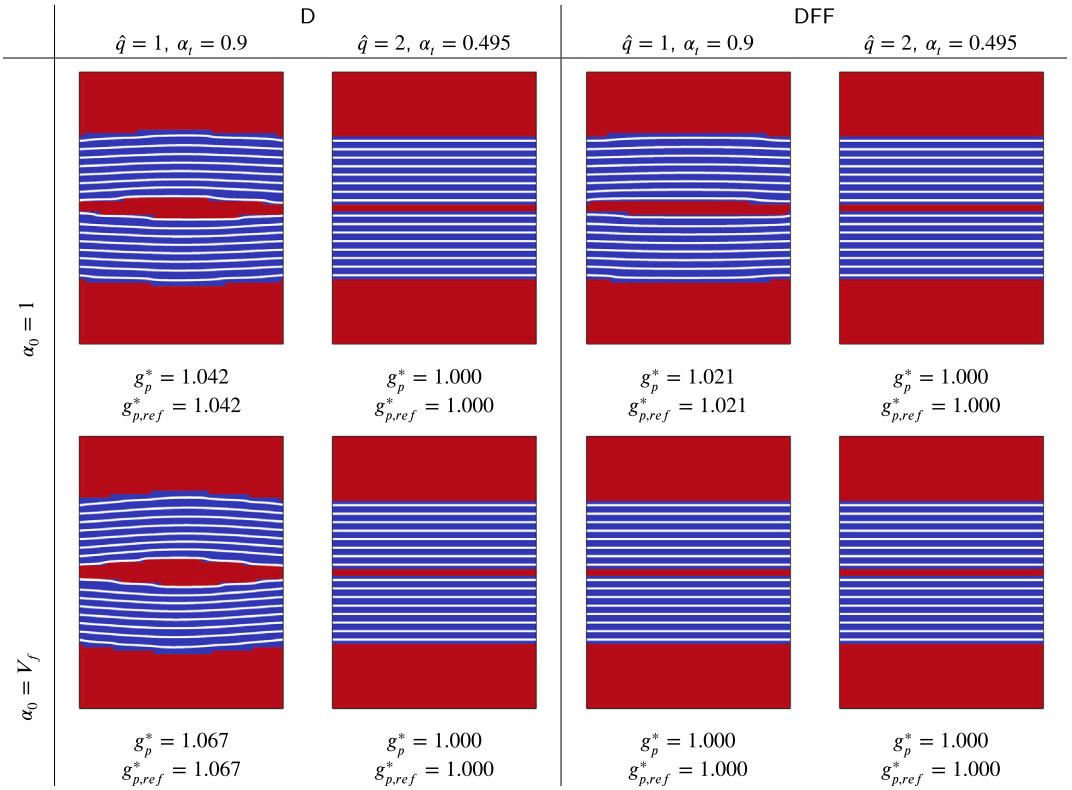

Fig. 12. Optimized designs computed using $L_c = L$ and associated raw objective value g_p^* and post-processed objective value $g_{p,ref}^*$ following Section 2.6 using α_t. Only the solution in the gray design domain in Fig. 6 is shown.

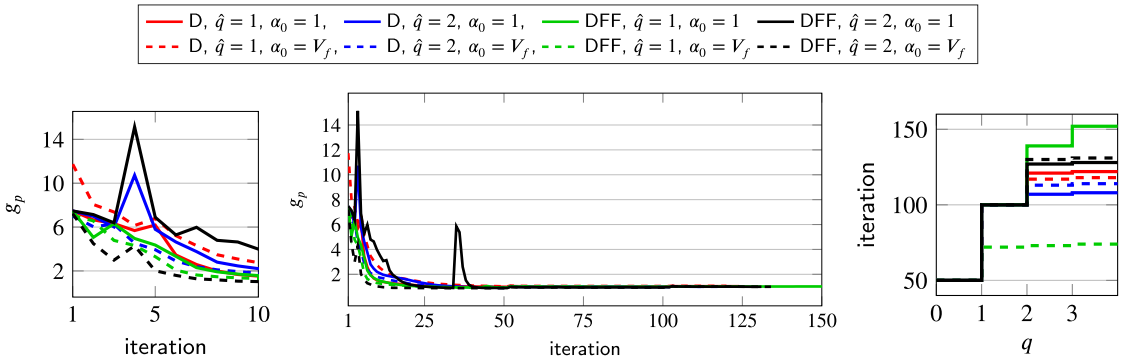

Fig. 13. The convergence history for the problem in Fig. 6 using $L_c = L$.

Comparing the DFF against the D results, it should be noted that while the DFF approach performs better, optimized designs still present bent channels which are suboptimal. As can be seen in Fig. 15, the convergence behavior of the DFF approach using $\hat{q} = 1$ is more stable and converges faster than the D approach. Large jumps and fluctuations are observed in the D objective after iteration 50 when we q is updated from 0 to 1. They are caused by the increase in q, which disturbs the objective by reducing the flow leakage through the solid domain, increasing the flow in the fluid domain and, consequently the pressure drop. To limit such disturbances a more gentle update of q is used in Section 5.2. Large objective fluctuations are only present in the DFF approach for $\hat{q} = 2$ during the initial convergence when using $q = 0$ in the first 25 design iterations.

In this section, we compared the D and DFF approaches with respect to their ability to escape ill-performing local optima. Optimization methods should balance accuracy of the solution, design flexibility, and convergence. The main issue of the D approach is a conflict between accuracy and design flexibility. As shown by the relatively large errors in objective Err_g found using the D approach in Fig. 14, a large Darcy penalization is needed for accuracy. However, a large penalization also results in the design

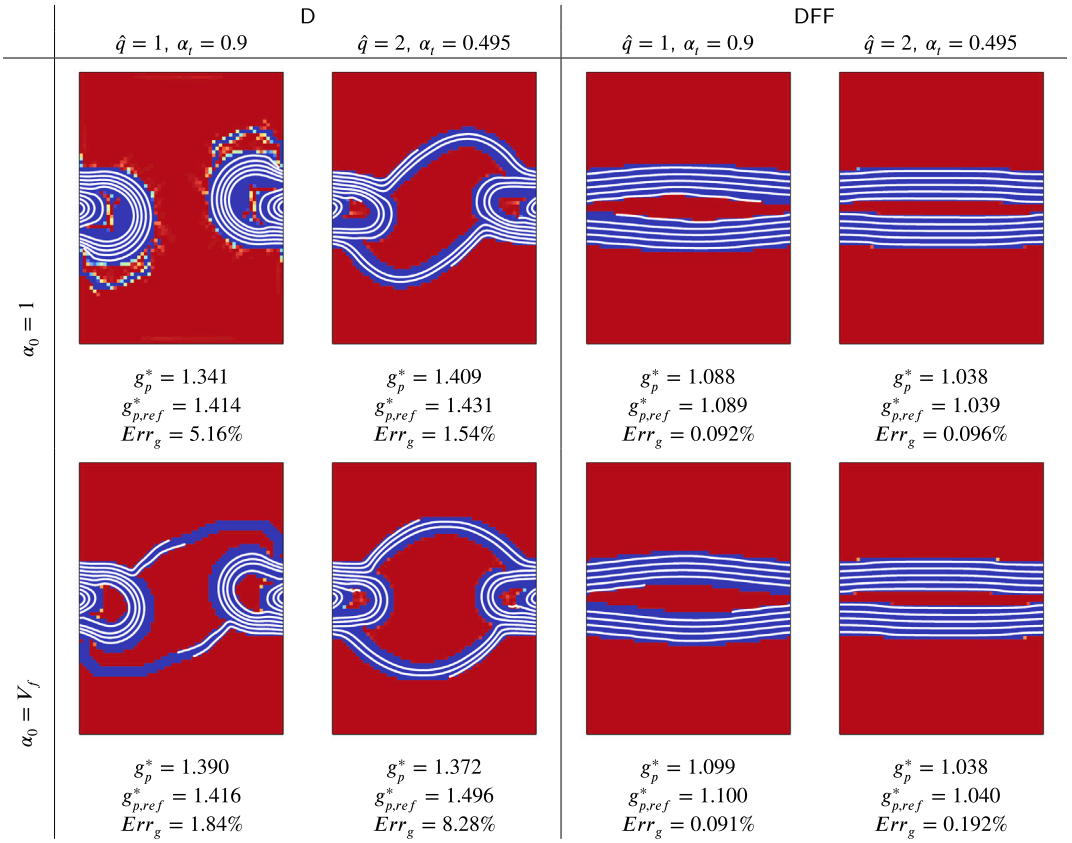

Fig. 14. Optimized designs computed using $L_c = L/2$ and associated raw objective value g_p^* and post-processed objective value $g_{p,ref}^*$ following Section 2.6. Only the solution in the gray design domain in Fig. 6 is shown. Relative errors in objective are defined as $Err_g = (g_{p,ref}^* - g_p^*)/g_{p,ref}^*$.

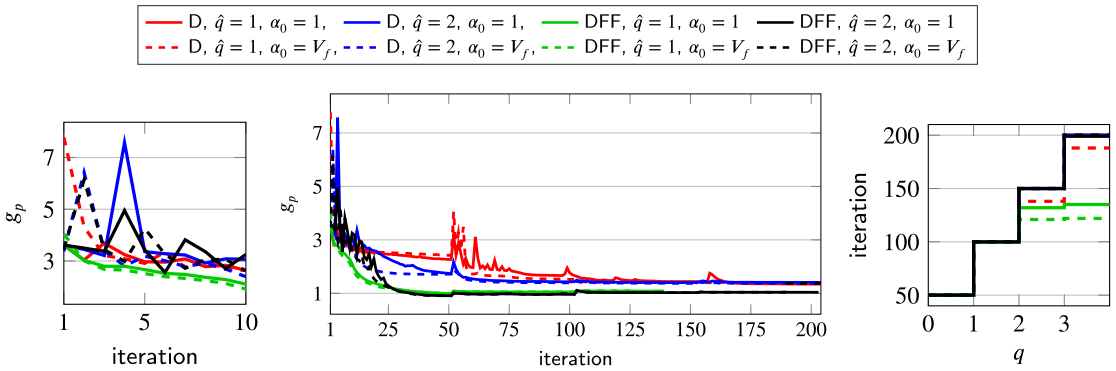

Fig. 15. The convergence history for the problem in Fig. 6 using $L_c = L/2$. Large fluctuations in objective are observed for the D approach after iteration 50 where we update q from 0 to 1.

converging to ill-performing local optima. This effect is less prevalent in the DFF approach which generally converges to better performing optima.

Another issue in both approaches is a conflict between design flexibility and convergence behavior. To avoid premature convergence to inferior local optima and promote design flexibility, the objective response is made more convex by lowering the penalization for gray design variables and using the higher $\hat{q} = 2$. However, the resulting interpolation function has a steep slope towards the maximum penalization, which often results in large design updates causing large changes in the flow solution and jumps in objective. Using a less steep interpolation function with $\hat{q} = 1$ results in smaller design updates, but a larger tendency to end up in ill-performing local optima.

5.2. Flow inverter

In more practical optimization problems, design domains are larger and flow velocities may vary more drastically. For example, a heat exchanger may present large velocities at the inlet, and relatively low velocities in many branching channels. To illustrate the benefits of achieving a predictable flow reduction in the DFF approach regardless of the local Re_e^f, we tackle a problem with inherently differing elemental Reynolds numbers. The problem is inspired by the flow inverter introduced by Gersborg-Hansen et al. [5] and recently used by Alexandersen [9]. It is assumed that by inverting the flow, velocities locally increase, causing elemental Reynolds numbers to increase and vary throughout the design domain. In the problem shown in Fig. 16, fluid generally flows from the inlet Γ_i, where a parabolic inflow with maximum velocity $\overline{v}$ is applied, to the outlet Γ_o, where a constant static pressure ($p_o = 0$) is applied. However, we optimize for the maximum amount of inverted flow in x-direction $-u_p$ at the center of the domain, and minimize:

$$g_v = 1 + \frac{u_p}{u_{p,max}}, \tag{65}$$

where $u_{p,max}$ is set to ten times the inlet velocity $u_{p,max} = 10\overline{v}$. We add the volume constraint in Eq. (64) and a constraint on the inlet pressure:

$$g_p = \frac{\frac{1}{L}\int_{\Gamma_i} p d\Gamma}{\overline{p}(\beta)} - 1 \leq 0, \tag{66}$$

where $\overline{p}$ is the maximum allowed pressure drop, dependent on the user-defined parameter β. We define the reference pressure drop $\overline{p}$ assuming a parabolic flow profile as:

$$\overline{p} = \frac{8\mu\overline{v}}{L^2}(1+\beta)5L, \tag{67}$$

where the pressure gradient defined as $\partial p/\partial x = 8\mu\overline{v}/L^2$ is multiplied by the length of inlet and outlet channel and we allow for β times the pressure drop in the gray design area of length $5L$. This pressure drop constraint is consistent with [9]. We use the parameters in Table 6 and a Reynolds dependent viscosity:

$$\mu = \frac{\rho\overline{v}L}{Re_{in}}. \tag{68}$$

As in this problem, a symmetric initial design tends to converge to an ill-performing local optimum [9], the design is initialized using the non-symmetric design with a thin wall on the bottom of the channel in Fig. 16. We first use $Re_{in} = 100$, $\beta = 30$, $h = L/50$ to compare the results to [9] and investigate the relation between design evolution and continuation approach. In a second application, we will use $Re_{in} = 200$, $\beta = 60$, $h = L/40$ to examine the effect of different estimations of velocity magnitude $\tilde{v}^f$ in the D approach.

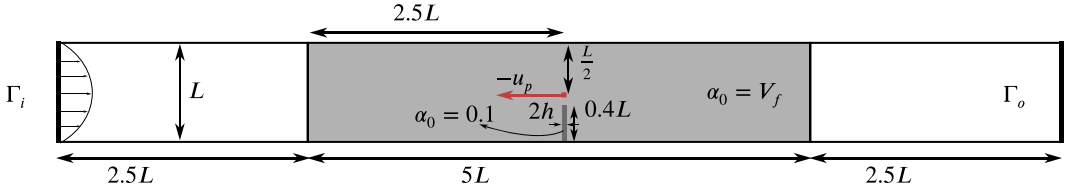

Fig. 16. The flow inverter optimization problem.

Table 6
Material and optimization parameters for the flow inverter in Fig. 16.

L	ρ	$\overline{v}$	$\tilde{v}^f$	N_i	q_{min}	q_{max}	Δq	$\hat{q}$	V_f
1 [m]	1 [kg m^{-3}]	1 [m s^{-1}]	$\overline{v}$	20	0	2	$\frac{1}{3}$	1, 2	0.6

5.2.1. Design evolution and continuation

At the optimum, the pressure drop constraint is generally active and a change in q may drastically perturb it. We thus use a more gradual continuation scheme for q and increase its value from $q_{min} = 0$ to $q_{max} = 2$ by small increments of $\Delta q = 1/3$ triggered every $N_i = 20$ design updates, as shown in Table 6. It should be noted that a maximum value $q_{max} = 2$ is selected for this problem, as increasing q further leads to more accuracy of the flow solution, but no significant design changes. For higher q, the pressure response becomes concave and the design does not change much compared to the one found using lower values of q. Moreover, for the D approach and to a lesser extent the DFF approach, using $q = 3$ often causes the flow solution to become unstable and design updates more erratic. Once the maximum value for $q = q_{max}$ is set after 120 iterations, the optimization process is allowed to take 80 extra iterations to perform final shape changes to the design.

We inspect the optimized designs and their convergence behavior. The designs, inverted flow magnitudes and inlet pressures in the optimized density-based design (u_p^*, p_{in}^*), and their reference values ($u_{p,ref}^*$, $p_{in,ref}^*$) computed using a post-processed design as described in Section 2.6, can be found in Fig. 17 for $\hat{q} = 1$ and Fig. 18 for $\hat{q} = 2$. We compute errors with respect to the post-processed reference designs as:

$$Err_u = \frac{u_{p,ref}^* - u_p^*}{u_{p,ref}^*} \qquad Err_p = \frac{p_{in}^* - p_{in,ref}^*}{p_{in,ref}^*},$$

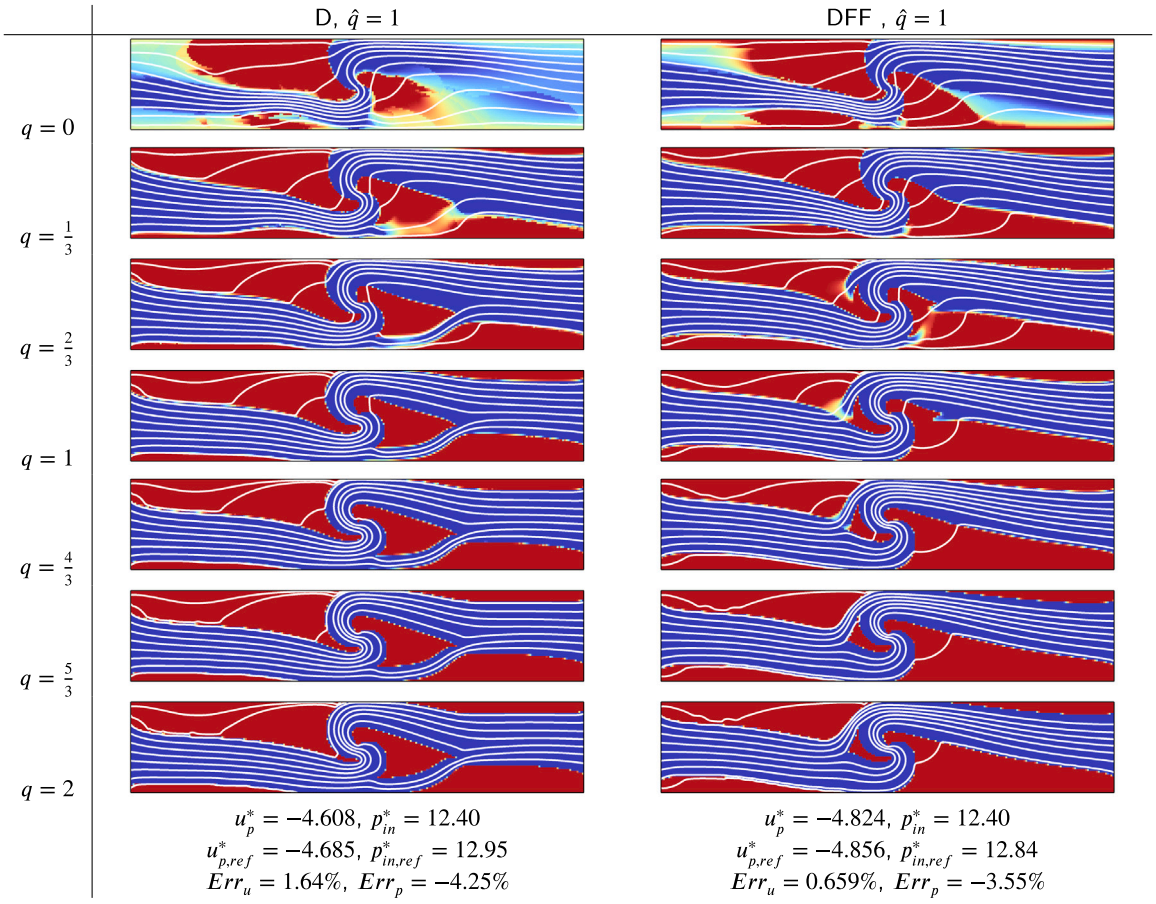

Fig. 17. The flow inverter designs including streamlines for $Re_{in} = 100$, $h = L/50$ and $\beta = 30$ at the end of each continuation step for q optimized using $\hat{q} = 1$. Only the solution in the gray design domain in Fig. 16 is shown. Inverted flow velocity and inlet pressure u_p^*/p_{in}^* at the optimum and their post-processed reference values $u_{p,ref}^*/p_{in,ref}^*$, computed using $\alpha_i = 0.45$ following Section 2.6, are given. Inlet pressures are constrained using $\bar{p} = 12.4$.

where a negative (resp. positive) error deteriorates (resp. improves) the design. Using $\hat{q} = 1$, the D and DFF approaches find similar performing optima with low errors Err_u, Err_p. Comparing our designs to [9], both the D and DFF approach find a similar topology. We note that our problem and continuation setup are different and we optimize using a higher maximum penalization than the one used in [9].

To examine the relation between the continuation and design evolution, we show the final design for each continuation step on q in Fig. 17 for $\hat{q} = 1$ and in Fig. 18 for $\hat{q} = 2$. Both approaches find a final topology for lower q after which only shape changes occur for higher q. However, for $\hat{q} = 1$ respectively $\hat{q} = 2$, the D approach generates the distinct fluid/solid topology for $q = \frac{2}{3}$ respectively $q = 1$, and the DFF approach for $q = \frac{4}{3}$ respectively $q = \frac{5}{3}$. The DFF approach settles to its final topology for designs with higher penalization and thus more accurate flow solutions. Using the higher $\hat{q} = 2$ allows the optimizer to keep changing the topology at higher penalization values. However, the final designs in Fig. 18 for $\hat{q} = 2$ contain more intermediate volume fraction elements at the boundaries. Porous solid/fluid interfaces are caused by the convexity of the pressure drop response, which was found in Section 4.2 to be undetermined for $\upsilon^s/\upsilon^f = 10^{\hat{q}-q} = 1$. We note that the optimal design found using the DFF approach with $\hat{q} = 1$ performs best.

Another distinction in design convergence is the fact that the DFF approach is able to introduce a fluid channel within a solid domain at later stages of the optimization procedure. For $q = \frac{1}{3}$, a solid domain is constructed in the top left half of the design, although significant flow is present in this porous solid domain. Over the subsequent iterations, the flow through the porous solid domain is inhibited, forcing the creation of new channels through these areas. The final topology is found at $q = 1$ and $q = \frac{4}{3}$ for $\hat{q} = 1$ and $\hat{q} = 2$, respectively. A rationale behind the evolving channels can be found by inspecting the pressure drop constraint in Fig. 19. At each increase in q, less flow is allowed in the porous solid domain and forced back into the fluid domain, resulting in an increase in the inverted flow magnitude and pressure drop. To counter this effect, side channels bypassing the flow inversion are introduced in areas of large flow leakage in the porous solid domain. For the D approach, the design evolution is straightforward. After finding its first distinct fluid/solid topology, only shape and no topology changes are performed. We note that in Fig. 18 for $\hat{q} = 2$, the D approach attempts to form a channel through the solid domain in the bottom left half of the design at $q = \frac{5}{3}$. However,

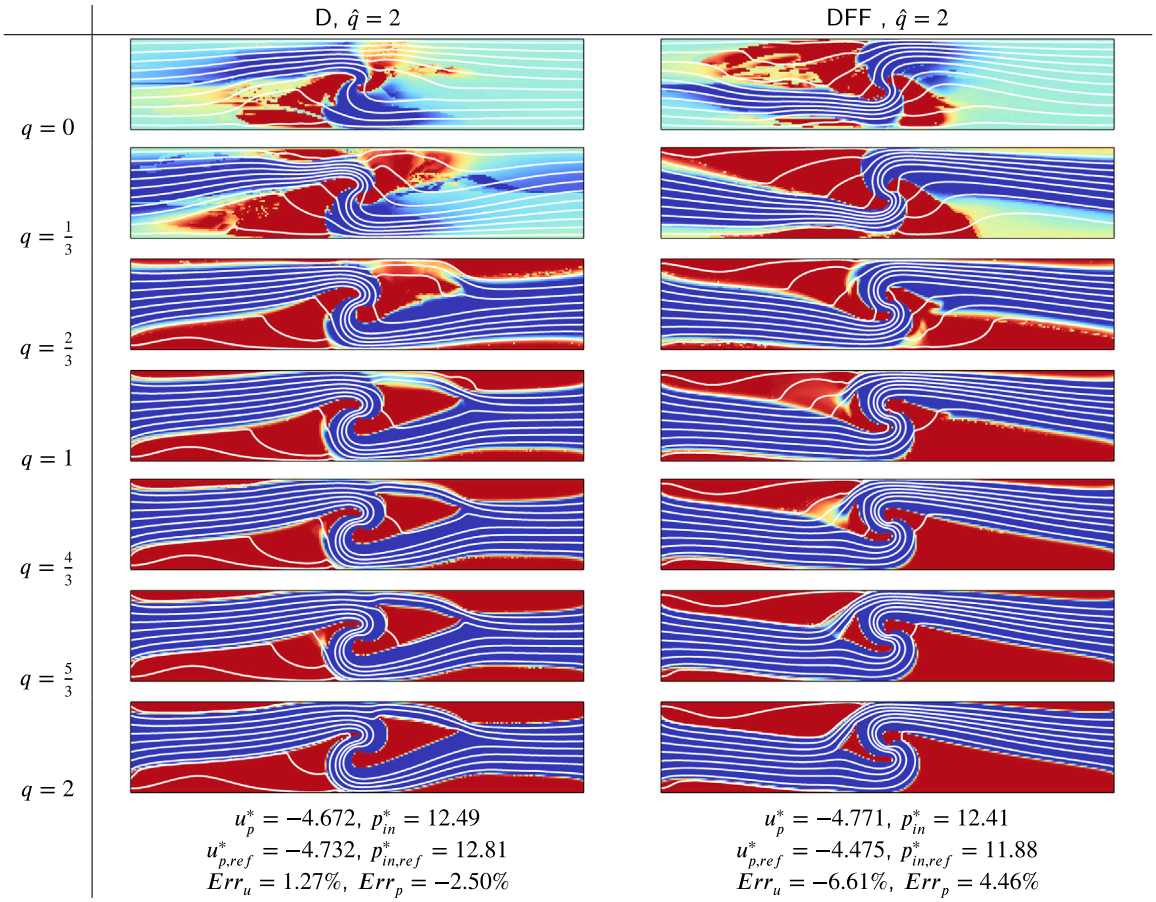

Fig. 18. The flow inverter designs including streamlines for $Re_{in} = 100$, $h = L/50$ and $\beta = 30$ at the end of each continuation step for q optimized using $\hat{q} = 2$. Only the solution in the gray design domain in Fig. 16 is shown. Inverted flow velocity and inlet pressure u_p^*/p_{in}^* at the optimum and their post-processed reference values $u_{p,ref}^*/p_{in,ref}^*$, computed using $\alpha_t = 0.082$ following Section 2.6, are given. Inlet pressures are constrained using $\bar{p} = 12.4$.

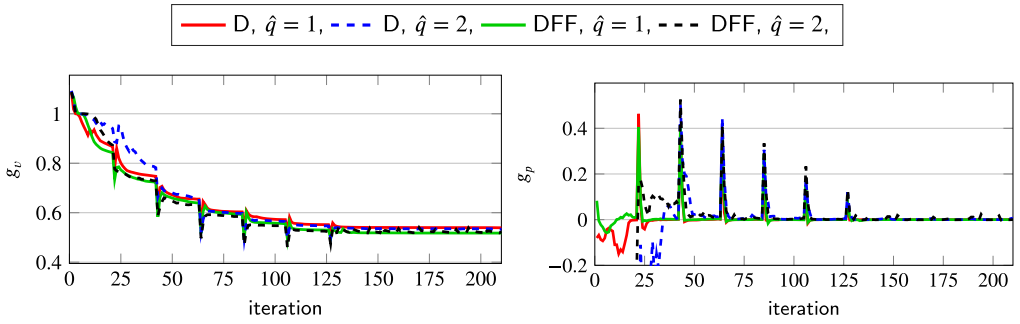

Fig. 19. The objective and the inlet pressure constraint for the flow inverter design computed with $Re_{in} = 100$ and $h = L/50$. We observe fluctuations in objective and constraint at each increase of q in our continuation.

the design change is too slow and increasing the penalization using $q = 2$ removes the channel from the design. The DFF approach is more flexible in the sense that even when the penalization and the consequent flow solution accuracy are increased, topology changes are more likely to occur.

5.2.2. Design convergence for differing estimations of the elemental Reynolds number

Although elemental Reynolds numbers were varying over the design domain in the previous example, they remained generally low. Using the maximum inlet velocity $v^f = \bar{v} = 1$ or the inverted flow magnitude $v^f = u_p \approx 5$, we find elemental Reynolds numbers

Table 7
The estimations for $\tilde{v}^f$ and consequent elemental Reynolds numbers and penalization magnitudes. Values are computed for the flow inverter using $Re = 200$ and $h = \frac{L}{40}$.

	D^-	D	D^+
$\tilde{v}^f$	$0.1\overline{v}$	$\overline{v}$	$10\overline{v}$
$\widetilde{Re}_e^f$	0.5	5	50
$\overline{D}_1$	$10^q \frac{\mu}{h^2} = 8 \cdot 10^q$	$10^q \frac{\mu}{h^2} Re_e^f = 40 \cdot 10^q$	$10^q \frac{\mu}{h^2} Re_e^f = 400 \cdot 10^q$

of $Re_e^f = 2$ or $Re_e^f = 10$, respectively. To investigate the convergence for higher elemental Reynolds numbers, we optimize the flow inverter for $Re_{in} = 200$ and $h = \frac{L}{40}$, which leads to an increase in pressure drop for similar inverted flow magnitudes. While the elemental Reynolds number at the inlet remain low, $Re_e^f = 5$, we allow for larger pressure by increasing β from 30 to 60, which should result in a higher elemental Reynolds number at the flow inversion of $Re_e^f \approx 25$.

To investigate the effect of the penalization on local features where flow speeds and thus elemental Reynolds number vary, we examine the effect of selecting different estimations of $\tilde{v}^f$ and associated elemental Reynolds number $\widetilde{Re}_e^f$. Varying the estimated flow velocity allows us to investigate the effect of an erroneous estimation as could be encountered in larger, more complex optimization problems. As shown in Table 7, we study the D approach for $\tilde{v}^f = 0.1\overline{v}$, $\overline{v}$, and $10\overline{v}$, referred to as the D^-, D, and D^+ approaches, respectively. Using $\tilde{v}^f = 0.1\overline{v}$ and $\widetilde{Re}_e^f = 0.5$, the dominant forces are expected to be viscous, and we penalize using $\overline{D}_1 = 10^q \mu / h^2$. Using $\tilde{v}^f = 10\overline{v}$ and $\widetilde{Re}_e^f = 50$, the penalization magnitude dependents linearly on the elemental Reynolds number as $\overline{D}_1 = 10^q \widetilde{Re}_e^f \mu / h^2$ and is two times larger than a penalization computed using $\tilde{v}^f = u_p \approx 5$ and $\widetilde{Re}_e^f = 25$. The D^+ approach thus uses a fair approximation when the actual maximum velocity magnitude in the design domain is taken into account. To illustrate the advantage of the DFF approach which does not rely on $\tilde{v}^f$, we compare designs optimized using the DFF approach against those optimized using the D^-, D, and D^+ approaches.

We compare the optimized designs, objective, and constraint in Fig. 20. The D and the DFF approaches show the best performance and find a similar design. The D^- and D^+ approaches yield ill-performing local optima associated with large errors Err_u and Err_p. In the D^- design, volume fraction $\alpha \approx 0.95$ is found for $q = 2$ in the area shown by the green circle. In this area with flow magnitudes around $v^f \approx 1.5$, the penalization is too low to force the channel to become completely fluid. Moreover, due to the high amount of flow leaking through the solid domains, objective and constraint values have large errors with respect to the reference simulation, computed using $\alpha_t = 0.45$ following Section 2.6. The cause of the excessive flow leakage is examined in Fig. 21 using the elemental Reynolds number in the optimized designs. For the D^- approach, the elemental Reynolds numbers abruptly decrease at the solid/fluid interface, and the solid domain significantly underestimates the fluid domain elemental Reynolds numbers. Consequently, the penalization based on $\widetilde{Re}_e^f < 1$ assumes viscous terms are dominant, whereas the higher inertial terms are dominant in the fluid domain where $Re_e^f > 1$.

The D^+ designs in Fig. 20 quickly converge to an inferior local optimum. Due to the high penalization, the design topology is identified using $q = 0$, and does not undergo any large modifications over subsequent continuation steps. The elemental Reynolds number is significantly overestimated in the solid domain as shown in Fig. 21. Moreover, with respect to the post-processed design. the D^+ design presents large errors Err_u and Err_p, which have two origins. Firstly, the design contains small, but crucial, features of only one element in size, which are gray ($\alpha \approx 0.5$) but have a relatively large impact on the flow. The optimizer is thus misusing the high penalization in intermediate density elements to improve the objective. Secondly, when post-processing using the approach in Section 2.6, we assume that a correct penalization is used, such that $v^s / v^f < 10^{-1}$ in the solid domain where $\alpha < \alpha_t$. However, due to the overestimation of the elemental Reynolds number and consequent over-penalization, the prediction of v^s / v^f becomes inaccurate. Consequently, we are not able to threshold the design appropriately. In general, issues related to the under- or over-estimation of the velocity become more significant when considering designs with many branching flow channels and differing flow magnitudes.

As we expect post-processing to be inaccurate due to erroneous estimations of $\widetilde{Re}_e^f$, an adapted post-processing approach for the D^- and D^+ designs is examined. In Eq. (47), we determine the threshold value as $\alpha_t = (1 - 10^{r-q})/(1 + 10^{r-q+\hat{q}})$, using a flow reduction in the solid domain of $v^s / v^f < 10^{-r}$. This value is based on an appropriate penalization magnitude and estimation of $\widetilde{Re}_e^f$. In all designs, we find $u_p \approx 5$ and we assume an appropriate estimation to be $\widetilde{Re}_e^f = 5$. For the D^- approach, the penalization is thus five times too low. To compensate for this underpenalization, the threshold value should be chosen at a penalization value which is five times higher than the one found at α_t. This is found using $r = 1$ at a threshold of $\tilde{\alpha}_t = (1 - 5 \cdot 10^{r-q})/(1 + 5 \cdot 10^{r-q+\hat{q}}) = 0.083$. For the D^+ design, a similar analysis results in a threshold of $\tilde{\alpha}_t = 0.9$. Using these threshold values, we find the errors with respect to the post-processed design to decrease in Fig. 20. This poses a challenge to post processing larger designs with many branching channels as an appropriate threshold value depends on a local elemental Reynolds number, and a unique threshold α_t may not exist.

The flexibility and stability of the design convergence are investigated by inspecting the objective and constraint convergence in Fig. 22. For the D^- approach, we find the objective to converge slowly over the first iterations. This is caused by the fact that the penalization is not high enough to sufficiently guide the flow and impact the design. For the D^+ approach, the objective decreases relatively quickly. After the $q = \frac{1}{3}$ continuation step, no large design changes happen and the main reduction in objective is caused by a reduction of the flow through the porous solid areas. Moreover, due to the high penalization, we observe oscillatory behavior of the pressure constraint, especially in the first 30 iterations. The D and DFF approaches both converge smoothly, except at the iterations where q is increased. The D^- approach is unable to accurately represent the design and the D^+ approach prematurely

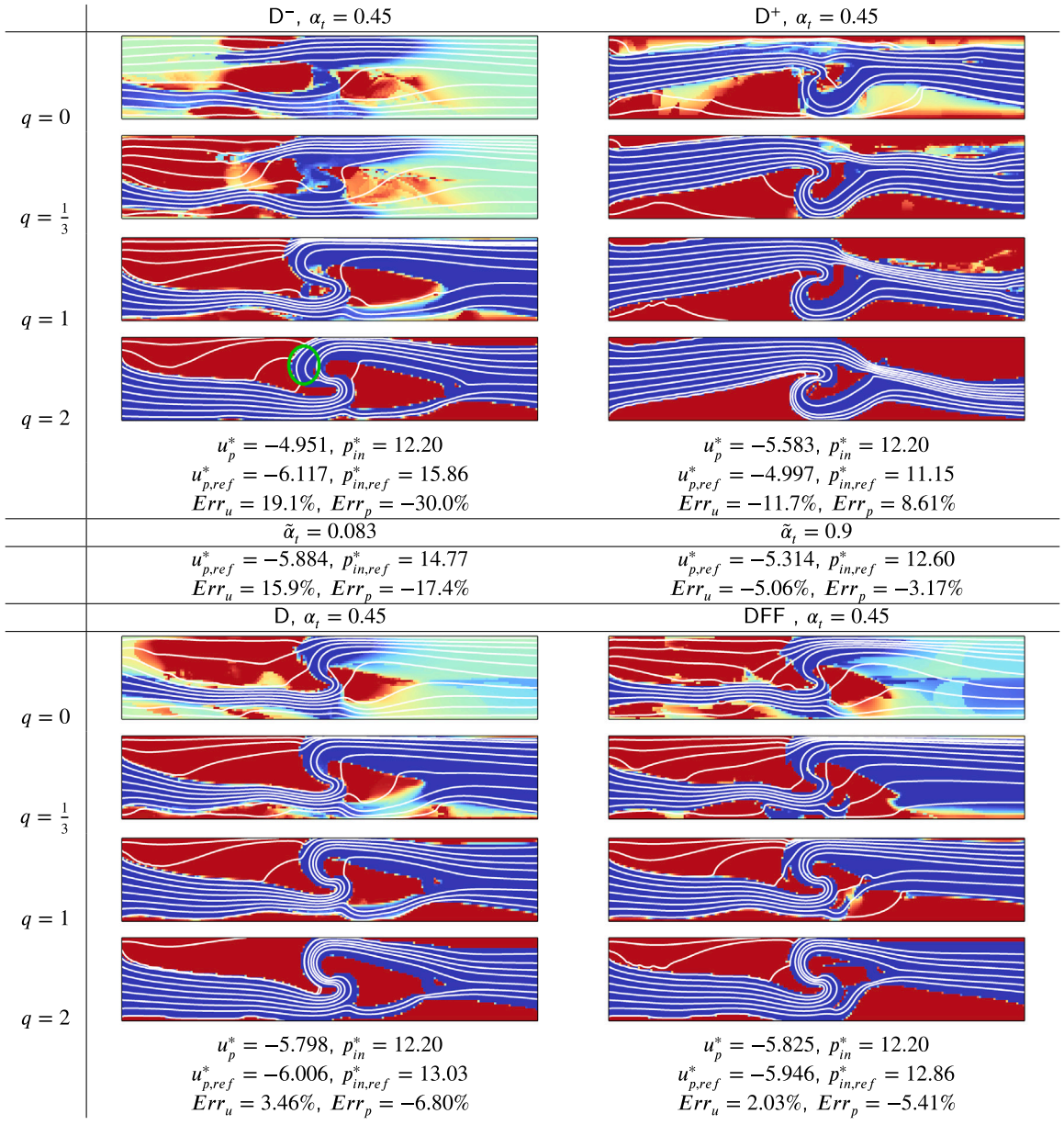

Fig. 20. The flow inverter designs including streamlines for $Re_{in} = 200$, $h = L/40$ and $\beta = 60$ at the end of continuation steps for q optimized using $\hat{q} = 1$. Only the solution in the gray design domain in Fig. 16 is shown. In the D⁻ $q = 2$ design, porous elements of volume fraction $\alpha \approx 0.95$ are found in the area denoted by the green circle. Inverted flow velocity and inlet pressure u_p^*/p_{in}^* at the optimum and their post-processed reference values $u_{p,ref}^*/p_{in,ref}^*$ are given. For the D⁻ and D⁺ results, we additionally post-process using updated threshold values $\tilde{\alpha}_t$, based on a compensation of the erroneous penalization magnitude. Inlet pressures are constrained using $\bar{p} = 12.2$. (For interpretation of the references to color in this figure legend, the reader is referred to the web version of this article.)

converges towards an ill-performing local optimum. This demonstrates that the tuning of the penalization in the D approach is both crucial and sensitive. However, the DFF approach requires no velocity estimate and shows design flexibility while the optimal design remains accurate.

6. Discussion

One of the main advantages of the Darcy with Filtered Forchheimer (DFF) approach is the reduced parameter tuning. While common approaches require trial-and-error to find an appropriate penalization magnitude, we select a penalization magnitude for a desired flow reduction of $v^s/v^f = 10^{-q}$ using Table 1. Moreover, we control convexity of the pressure drop response using both the penalization magnitude with q, and the penalization interpolation with $\hat{q}$. The DFF approach does not require tuning based on

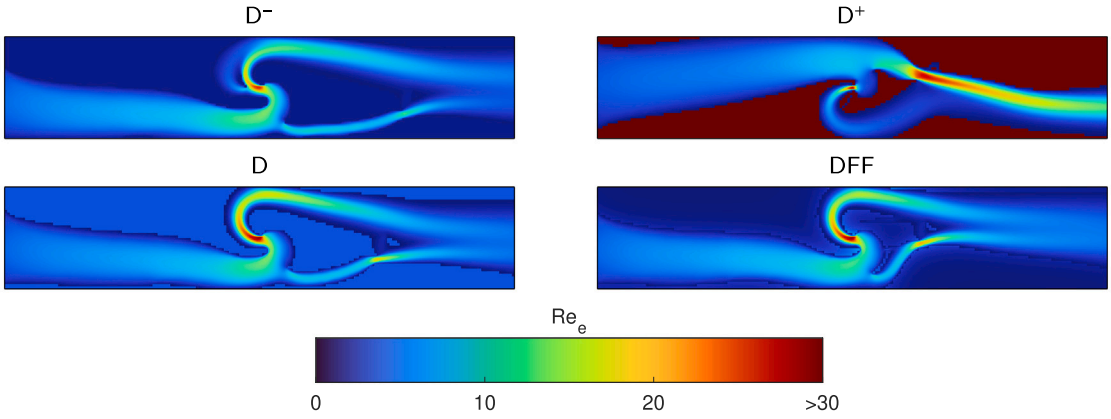

Fig. 21. Elemental Reynolds numbers in the designs for $q = 2$ from Fig. 20. In the fluid domain we plot $Re_e^f = (\rho|\mathbf{v}|_2 h)/\mu$. For the DFF approach we plot $Re_e^f = (\rho U h)/\mu$ in the solid domain. For the D, D$^-$, and D$^+$ approaches, we approximate and plot the constant $\widetilde{Re}_e^f$ as found in Table 7 in the solid domain. For D$^+$ approach, the solid domain elemental Reynolds number is $\widetilde{Re}_e^f = 50$, but the color-scale is limited to 30 for enhanced readability.

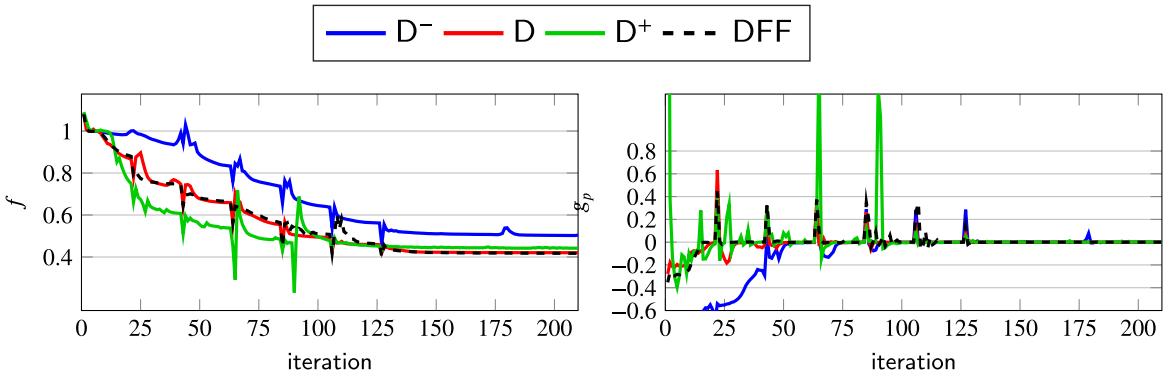

Fig. 22. The objective and the inlet pressure constraint for the flow inverter design computed with $Re_{in} = 200$ and $h = L/40$.

simulation results, but allows engineers to make an informed selection of the appropriate penalization based on a desired balance between flow solution accuracy and objective convexity. In practice, we recommend using $\hat{q} = 1$ and control convexity of the pressure drop response using q. Subsequently, a continuation on q can be derived starting with $q < \hat{q}$, to create a convex pressure drop response, and ending with $q > \hat{q}$, to create a concave pressure drop response. We recommend to initialize the optimization using $q = 0$ and finalize using $q = 2$. While choosing $q > 2$ decreases the flow leakage, we generally found the pressure drop response to become too concave for effective design updates. The update on q should be done in small increments to avoid destabilizing the design process. We found that increasing q by $\Delta q = 1/3$ every $N_i = 20$ design iterations performed well for the relatively unstable flow inverter design. However, more efficient continuation strategies are suggested as a subject for future research.

As discussed in Appendix A, the filter radius is defined in terms of number of elements N, which should not change for a different element size. Although an appropriate penalization can also be defined for a different number of elements N, tuning this parameter is not recommended. The main parameter determining the order of magnitude of the penalization is q. As a continuation on q is proposed, the required accuracy of the filtered velocity field is relaxed. A radius within $6 \leq N \leq 12$ elements will have enough accuracy for the continuation approach to work and the final design to be accurate.

The most common continuation strategy in flow TO is to start the optimization procedure with a highly convex penalization interpolation, i.e., equivalent to high $\hat{q}$ in this paper, and to finalize the optimization process using a less convex interpolation function, i.e., low $\hat{q}$ in this paper. We verified that the convexity of the pressure drop objective depends on the penalization magnitude in the gray areas of intermediate volume fraction. A highly convex interpolation function with a steep slope towards the maximum penalization has the same effect as the low maximum penalization used in this work, as both reduce the penalization in gray areas. However, using a steep slope in the penalization interpolation often causes design updates to become more erratic. A small change in design variable may have a large effect on the flow solution due to a sudden high penalization, which can drastically change the flow solution over design iterations due to the non-linear nature of the Navier–Stokes equations. For this reason, we prefer to use a continuation on the penalization magnitude instead of on the penalization interpolation. However, hybrid methods which apply a continuation on both the penalization interpolation and magnitude may be derived using the convexity analysis and the prediction of flow reduction in this paper.

As a first attempt at using the Forchheimer penalization previously introduced by Alonso and Silva [1], the Darcy with Forchheimer (DF) approach was introduced which improves on previous work by using an order analysis for the appropriate penalization magnitude. Although the DF approach is found to more reliably predict the flow reduction than the DFF approach, it also suffers from unstable flow solutions. Unstable flow solutions are mainly caused by reusing the state solution over subsequent design iterations, as reusing the state solution significantly decreases the computational effort. In the authors' experience, when attempting optimization using the DF approach, more erratic design updates are encountered, increasing the tendency to find diverging flow solutions when reusing the state solution. Furthermore, we note that the DF approach can be seen as a special case of the DFF approach where the velocity is averaged over a radius $R = 0$, and the penalization magnitude is increased. A hybrid between the DF and DFF approaches could thus be derived. Using a smaller filter radius R, the averaged flow magnitude will underestimate the fluid domain flow magnitude $U < v^f$, which may be compensated by using a higher maximum Forchheimer penalization $10^q \rho/h < \overline{F} < 10^{2q} \rho/h$. Using this approach, a novel method may be derived which is as stable as the DFF approach and finds accurate flow reductions as the DF approach.

The presented study on laminar moderate Reynolds flow TO is a first step towards improved understanding of turbulent high Reynolds flow TO. For future work, we recommend a similar procedure to derive an appropriate penalization strategy for turbulent flow TO using Reynolds Averaged Navier–Stokes (RANS) equations. The procedure should follow three steps: (1) A dimensional analysis on the discretized physics, similar to the one presented in Section 2. (2) The flow reduction and other turbulent boundary conditions at the solid/fluid interface are verified using an analysis similar to Section 4.1. (3) The convexity of the objective response is inspected using a method similar to Section 4.2. As turbulent flow inherently contains high Reynolds numbers, we expect the DFF approach to be required to appropriate penalize the RANS momentum equation. Moreover, a similar procedure to derive a robust TO approach may be performed for other problems. An example is TO problems involving thermo-fluid equations which often require tuning to find appropriate material interpolation functions. To this end, we introduced a more general analysis approach in Section 2.1 than the one presented in [14]. While the analysis in [14] is specific for flow physics and relies on the continuous pressure gradient, the analysis in this work can be extended to penalization or interpolation approaches for different physics.

7. Conclusion

To derive a reliable penalization approach for moderate Reynolds flow TO, the Forchheimer penalization is crucial. While the flow in areas where viscosity is dominant, is inhibited using the Darcy penalization, to penalize the flow in areas where inertia is dominant, the Forchheimer penalization is used. The Darcy penalization alone cannot simultaneously penalize the flow in both areas appropriately.

A reliable penalization and continuation approach for density-based TO of laminar moderate Reynolds flow problems has been introduced and compared to the state-of-the-art. The novel DFF approach is based on a Forchheimer penalization dependent on a filtered velocity, and a continuation strategy with a predictable flow reduction in the solid domain. Moreover, the approach does not depend on a specific problem setup, as it can be used without additional tuning to optimize different inlet/outlet configurations with different Reynolds numbers, and different mesh sizes. We improve all four conditions, stated in Section 1, for a reliable approach as follows: (1) Continuing our previous work in [14], parameter tuning is reduced by deriving appropriate penalization magnitudes for a predictable flow reduction. (2) As the flow reduction is predictable in the DFF approach, we can guarantee its value and that the flow solution is accurate in the optimal design. (3) By analyzing the convexity of the pressure drop response, a continuation strategy is derived for both the D and the DFF approach which mitigates the tendency to converge to ill-performing local optima. By starting the optimization procedure with a low penalization, the pressure drop response is convex and the design easily changes. Subsequently, the maximum penalization is increased making the pressure drop response concave and forcing the design into a discrete solid/fluid solution. (4) Although no thorough analysis is performed on the stability of the flow solution, we found relatively quickly and reliably converging flow solutions for both the D and the DFF approach.

CRediT authorship contribution statement

M.J.B. Theulings: Writing – review & editing, Writing – original draft, Visualization, Software, Methodology, Investigation, Formal analysis, Conceptualization. **L. Noël:** Writing – review & editing, Supervision. **M. Langelaar:** Writing – review & editing, Supervision. **R. Maas:** Writing – review & editing, Supervision.

Declaration of competing interest

The authors declare that they have no known competing financial interests or personal relationships that could have appeared to influence the work reported in this paper.

Appendix A. Filter size for the Darcy with filtered Forchheimer approach

We investigate the effect of the filter size R on the flow reduction in the DFF approach. A predictable flow reduction is desirable as the continuation approach in Section 5 allows for more leakage and design flexibility in the first design iterations, and less leakage

resulting in accurate and crisp but less flexible designs in the final design iterations. We require the filter to be large enough such that the filtered velocity magnitude U in solid elements accurately represents the velocity magnitude in neighboring fluid elements, i.e., $U \approx v^f$. For $Re_e^f > 1$, underestimating the fluid velocity magnitude $U \ll v^f$, leads to an underestimated Forchheimer magnitude and results in increased flow leakage, $v^s/v^f > 10^{-q}$. Overestimation $U \gg v^f$ leads to an overestimated Forchheimer magnitude, resulting in reduced flow leakage, $v^s/v^f < 10^{-q}$. We intend to find the appropriate filter radius $R = Nh/(2\sqrt{3})$, which determines the distance over which information is distributed. The radius is defined using N, the number of elements of size h in radius R [22].

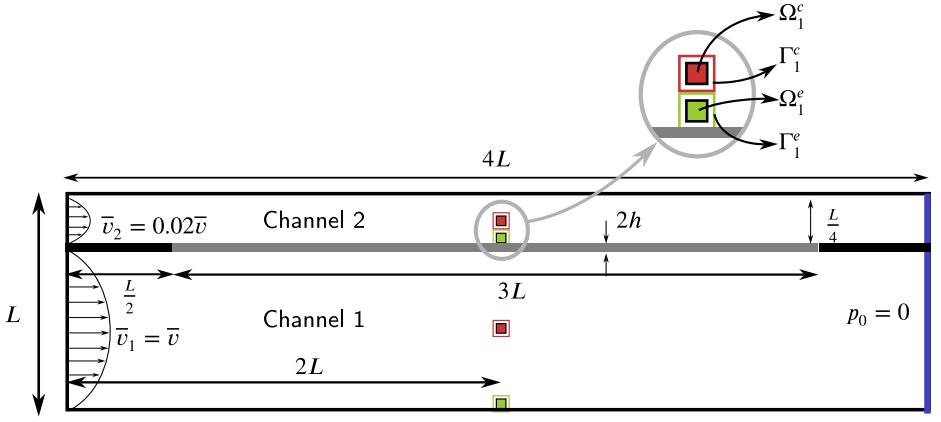

Fig. 23. Design for testing the effect of different filter radii R on the predictability of the flow reduction in the DFF approach. The design is split into Channel 1 at the bottom with relatively large velocity magnitudes, and Channel 2 at the top with relatively low velocity magnitudes. The separating wall consists of a solid part (black), where velocity is fixed as $\mathbf{v} = \mathbf{0}$, and a density-based part (gray), where flow is inhibited such that $v^s \ll v^f$. At the midpoint of both channels, density-based obstacles of size $2h$ by $2h$ are placed at the edge (Ω_i^e in green) and in the center (Ω_i^c in red). Separated by one element from the obstacles, boundaries Γ_i^c and Γ_i^e are defined to measure the velocity magnitudes in neighboring fluid elements. (For interpretation of the references to color in this figure legend, the reader is referred to the web version of this article.)

The design in Fig. 23 is used to inspect flow leakage for several filter radii. Two channels separated by a two-element thick porous wall are investigated. In Channel 1 at the bottom, flow speeds are high with a maximum inlet velocity of $\overline{v}_1 = \overline{v}$, in Channel 2 at the top, they are low with $\overline{v}_2 = 0.02\overline{v}$. We expect U to overestimate v^f in the top channel when the filter radius is too large, as U will be influenced by the large flow magnitude in the bottom channel. The parameters in Table 8 are used and we inspect two different mesh sizes, $h = \frac{L}{40}$ and $\frac{L}{80}$. A Reynolds dependent density ρ, in Eq. (58), is used. We emphasize that the different mesh size influences the filter radius as it is dependent on a number of elements N. We thus compute the flow solution for varying N, and expect to find the appropriate N, independent of the mesh size h.

Table 8
Parameters used to measure the effect of the filter radius in flow leakage for the design in Fig. 23.

L	Re_{in}	μ	$\overline{v}$
1 [m]	4000	1 [N s m^{-2}]	10 [m s^{-1}]

To inspect the flow leakage, we introduce obstacles in the flow at the edges and in the centers of the channels. Flow leakage is computed using Eq. (59). Edge and center obstacle have domains Ω_i^e and Ω_i^c, both with area A_Ω, and boundary Γ_i^e and Γ_i^c with length L_Γ^e and L_Γ^c, respectively. Beside the leakage, we inspect the accuracy in filtered flow magnitude U with respect to the measured fluid velocity magnitude:

$$\widetilde{U}_i^e = \frac{U}{v^f} \approx \frac{\int_{\Omega_i^e} U\, d\Omega}{\int_{\Gamma_i^e} |\mathbf{v}|_2 d\Omega} \frac{L_\Gamma^e}{A_\Omega}, \qquad \widetilde{U}_i^c = \frac{U}{v^f} \approx \frac{\int_{\Omega_i^c} U\, d\Omega}{\int_{\Gamma_i^c} |\mathbf{v}|_2 d\Omega} \frac{L_\Gamma^c}{A_\Omega} \tag{69}$$

For accuracy close to 1, the filtered velocity magnitude U accurately represents the fluid velocity magnitude v^f and the filtered Forchheimer penalization should lead to the expected flow leakage of $v^s/v^f = 10^{-q}$.

To measure the effect of the filter radius on the filtered Forchheimer penalization, we require it to be dominant and thus $Re_e^f \approx Re_e^s > 1$. In Fig. 24, we show elemental Reynolds numbers in the channels for the most accurate flow solution computed using $q = 3$, $N = 16$, and $h = L/80$. In the fluid ($\alpha = 1$) and the solid ($\alpha = 0$) domain, elemental Reynolds numbers are computed as:

$$Re_e^f = \frac{\rho |\mathbf{v}|_2 h}{\mu}, \qquad Re_e^s = \frac{\rho U h}{\mu}. \tag{70}$$

Consequently, in Channel 1 we find elemental Reynolds numbers of $Re_e^f \approx 34$ at the center and $Re_e^f \approx 7.4$ at the edge obstacles, and in Channel 2, of $Re_e^f \approx 0.60$ and $Re_e^f \approx 0.39$, respectively. In bottom Channel 1, erroneous estimations of $U \approx v^f$ cause an

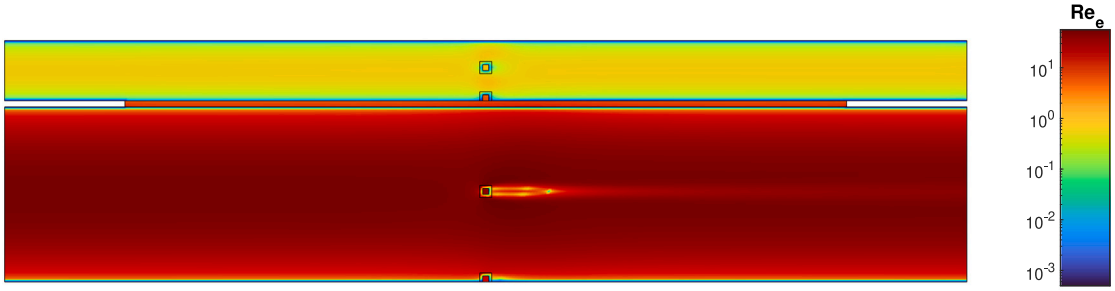

Fig. 24. Elemental Reynolds numbers in the fluid and solid domains for $q = 3$, $N = 16$, and $h = L/80$.

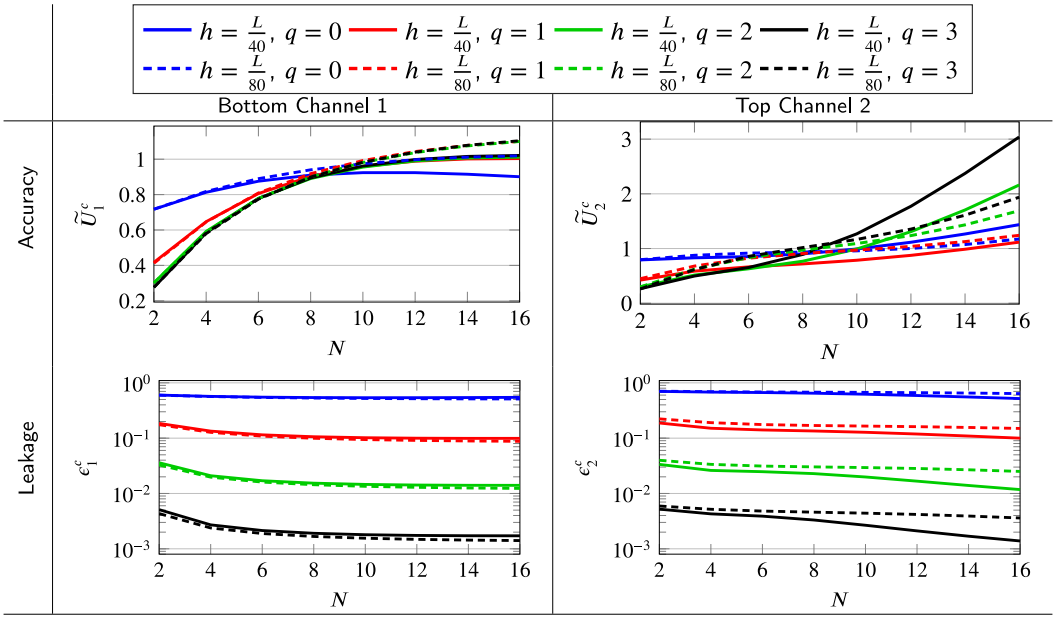

Fig. 25. The flow leakage and filtered velocity magnitude accuracy for the center obstacles Ω_i^c.

inappropriate penalization and less predictable flow leakage. In top Channel 2, underestimating $U < v^f$, resulting in $Re_e^s < Re_e^f < 1$, renders the Darcy penalization dominant, which should accurately penalize the dominant viscosity in the fluid domain. However, overestimating $U > v^f$ may cause $Re_e^s > 1$, resulting in a dominant Forchheimer penalization with a larger magnitude than the appropriate Darcy penalization.

In Fig. 25, the measured leakage and filtered velocity accuracy for the center obstacles can be found. At the center island in Channel 1, the accuracy $\widetilde{U}_1^c$ tends to 1 for filter radii containing more elements, which leads to a predictable flow reduction $v^s/v^f = 10^{-q}$. In Channel 2, the accuracy in filtered flow magnitude is overestimated for $N > 8$. The filter radius is too large and the flow velocity in bottom Channel 1 starts to influence the filtered velocity magnitude in top Channel 2. The overestimation of local flow speeds subsequently causes the flow leakage to decrease. The overestimation in the filtered velocity magnitude is more pronounced for $h = L/40$. This is caused by the fact that the center island is six elements away from the bottom channel for $h = L/40$ and 11 elements for $h = L/80$. A filter radius with less elements N thus results in the filter penetrating the bottom channel earlier for $h = L/40$ than $h = L/80$.

For the edge obstacles, overestimation of fluid flow velocities due to large filter radii poses a larger problem, as shown in Fig. 26. For the obstacle next to the solid bottom wall in Channel 1, increasing the filter radius past $N = 8$ elements results in an overestimation of the fluid flow velocity $\widetilde{U}_1^e > 1$. This causes the flow leakage to decrease below the expected value $v^s/v^f < 10^{-q}$. In top Channel 2, $\widetilde{U}_2^e$ increases even more drastically, but this does not cause a significantly larger flow reduction. When velocity magnitudes in the bottom channel dominate the filtered velocity in the top channel edge obstacle, the filtered velocity largely overestimates the local fluid velocity magnitude. However, flow in the edge obstacle is influenced by the bottom channel as flow passes through the porous wall into the edge obstacle. For the parabolic flow profile over the bottom inlet with maximum velocity $\overline{v}_1 = 10\ ms^{-1}$, the velocity magnitude at a distance h from the wall is theoretically 1.38 or 0.678 for $h = L/40$ or $h = L/80$, respectively. However, when we compute the average velocity magnitude around the edge obstacle in the top channel for $q = 3$, we

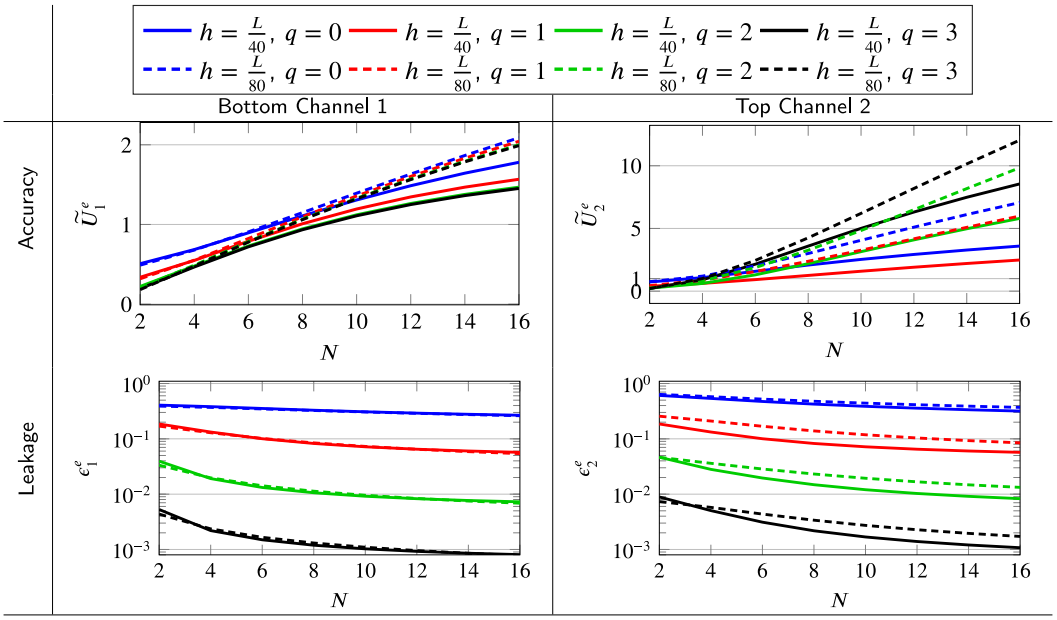

Fig. 26. The flow leakage and filtered velocity magnitude accuracy for the edge obstacles Ω_i^e.

find $0.29 > v^f > 0.19$ and $0.088 > v^f > 0.077$ for $h = L/40$ and $h = L/80$, respectively. Forces in the Navier–Stokes equations scale with velocity magnitude. Fluid domain forces below the wall will thus be larger than those above the wall. Consequently, the flow through the wall and in the edge obstacle next to the wall will be mostly dependent on the velocity magnitude below the wall.

To determine the appropriate number of elements N in the filter, we compare the different flow leakage results. A larger N is expected to distribute sensitivities more equally between the fluid and solid domain and to improve design convergence. Small changes may drastically alter the nonlinear flow solution and objective, smoothing out sensitivities and making design changes more gradual can improve design convergence. We thus choose the largest N for which no significant overpenalization occurs. Moreover, in the choice of filter radius, the results in Fig. 26 in top Channel 2 are neglected. The velocity magnitude in a solid domain is always determined by the largest velocity magnitude in the adjacent fluid domain. Consequently, overestimation of U only matters compared to the largest fluid domain velocity magnitude. Which is one of the major drawbacks of all penalization approaches presented in this paper. In two fluid areas separated by a thin solid domain, flow leaking from an area with high flow velocity to an area with low flow velocity significantly disturbs the flow in the latter area. In bottom Channel 1 in Fig. 26, a small amount of overpenalization occurs for $N = 10$, in Fig. 25, $N = 10$ results in an appropriate penalization. In this work, we thus use $N = 10$ to determine the filter radius for averaging the velocities.

Appendix B. Instability of the Darcy with Forchheimer approach

During optimization, we often found the DF approach to become unstable due to large fluctuations in design and the forward solution diverging. In this section, we investigate the cause of this instability in the DF approach and motivate our preference for the DFF approach.

The forward solve is a computationally expensive and time consuming part of the optimization process. The overall optimization time can be significantly reduced by decreasing the time spent on the forward solve. In this work, we use the forward solution in the previous design as the initial guess for the solution in the current design. However, reusing the previous flow solution may lead to instabilities, particularly in the DF approach. When solid material is introduced in areas previously filled with fluid, the initial guess based on this previous design significantly overestimates the flow magnitude in the current design, which may lead to instabilities in the forward solve. Consequently, instabilities are amplified by the larger design fluctuations more often found when optimizing using the DF approach than using the DFF approach. Moreover, as shown in this section, for the DFF approach this does not lead to diverging flow solutions, contrary to the DF approach.

To examine the effect of reusing the flow solution when sudden changes in design happen, we use the problem in Fig. 27. A thin solid fin is inserted in the middle of a flow channel with parabolic flow inlet and constant pressure outlet. We use the parameters in Table 9 and the Reynolds-dependent density from Eq. (58). The design is changed by extending the solid fin upstream, such that solid material is added in an area with large velocity magnitudes. We first solve the problem using the short fin, and subsequently reuse this flow solution to solve for the extended fin. We expect instabilities to be mainly caused by large elemental Reynolds numbers. A large $Re_{in} = 1000$ is thus used to ensure the large Re_e^s found in Fig. 29(a) for the DF approach.

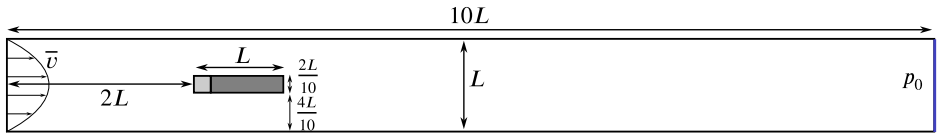

Fig. 27. The fin in a channel used to investigate forward solve instabilities. In the fluid domain (white), no penalization is present and in the solid domain (dark gray), the maximum penalization is present. At the tip of the fin, we change the fluid volume fraction α and thus the penalization in the two-by-two element sized light gray domain.

Table 9
Parameters used to investigate the instability of the DF approach using the problem in Fig. 27.

L	μ	$\bar{v}$	p_0	Re_{in}	q	h
1 [m]	1 [N s m^{-2}]	1 [m s^{-1}]	0 [Pa]	1000	2	$\frac{L}{10}$

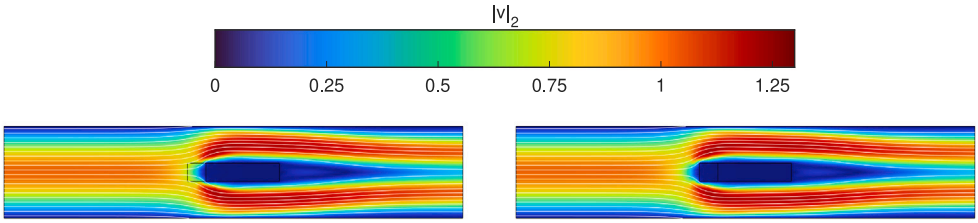

(a) Without extended fin. **(b)** With extended fin.

Fig. 28. The flow magnitude $|\mathbf{v}|_2$ and flow lines found using the DFF approach in the first half of the channel.

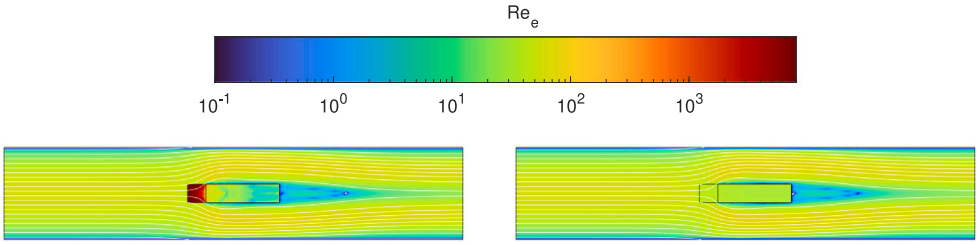

(a) DF approach **(b)** DFF approach

Fig. 29. Flow lines and elemental Reynolds number in the first forward iteration of the extended fin problem. In the fluid domain we plot $Re_e^f = (\rho|\mathbf{v}|_2 h)/\mu$, while in the solid domain we plot $Re_e^s = 10^q(\rho|\mathbf{v}|_2 h)/\mu$ for the DF approach and $Re_e^s = (\rho U h)/\mu$ for the DFF approach.

While the forward solution of the extended fin in Fig. 28 converges using the DFF approach, it diverges using the DF approach. When initializing using the flow solution of the problem without extended tip, the elemental Reynolds number for the DF approach in the extended tip is high relative to the elemental Reynolds number in the surrounding fluid, as shown in Fig. 29. For the DFF approach the elemental Reynolds number varies more smoothly. As described in Section 2.4, the fluid domain elemental Reynolds number $Re_e^f = (\rho v^f h)/\mu$ should be similar to neighboring solid domain elemental Reynolds number $Re_e^s = 10^q(\rho v^s h)/\mu$. To compensate for the jump in elemental Reynolds number in the DF approach, the fluid domain elemental Reynolds number is increased by increasing the fluid domain velocity magnitude v^f in the first forward iteration, as shown in Fig. 30(a). Subsequently, the flow solution does not stabilize. The abrupt change in elemental Reynolds number, caused by reusing the state solution after a sudden design change, destabilizes the forward solution in the DF approach. Contrarily, using the DFF approach, the velocity magnitude is significantly decreased in the solid tip after the first forward iteration and velocity magnitudes in the surrounding fluid area are not drastically increased, as shown in Fig. 30(b). This results in convergence of the forward solution even when initializing using an inaccurate initial guess in the DFF approach.

Data availability

Data will be made available on request.

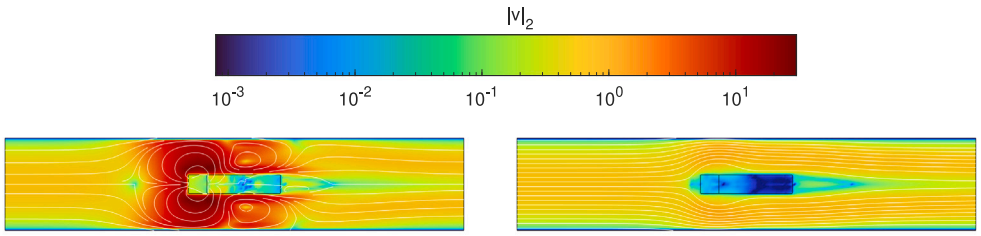

(a) DF solution. **(b)** DFF solution.

Fig. 30. Velocity magnitude $|\mathbf{v}|_2$ and flow lines in the extended fin problem after performing one nonlinear solution iteration. Instead of decreasing the relatively high flow in the tip, the flow around the tip is significantly increased.

References

[1] D.H. Alonso, E.C.N. Silva, Topology optimization applied to the design of tesla-type turbine devices, Appl. Math. Model. 103 (2022) 764–791.
[2] C.S. Andreasen, A.R. Gersborg, O. Sigmund, Topology optimization of microfluidic mixers, Internat. J. Numer. Methods Fluids 61 (5) (2009) 498–513.
[3] T. Kondoh, T. Matsumori, A. Kawamoto, Drag minimization and lift maximization in laminar flows via topology optimization employing simple objective function expressions based on body force integration, Struct. Multidiscip. Optim. 45 (5) (2012) 693–701.
[4] T. Borrvall, J. Petersson, Topology optimization of fluids in Stokes flow, Internat. J. Numer. Methods Fluids 41 (1) (2003) 77–107.
[5] A. Gersborg-Hansen, O. Sigmund, R.B. Haber, Topology optimization of channel flow problems, Struct. Multidiscip. Optim. 30 (2005) 181–192.
[6] L.H. Olesen, F. Okkels, H. Bruus, A high-level programming-language implementation of topology optimization applied to steady-state Navier–Stokes flow, Internat. J. Numer. Methods Engrg. 65 (7) (2006) 975–1001.
[7] T. Bruns, Topology optimization by penalty (TOP) method, Comput. Methods Appl. Mech. Engrg. 196 (45–48) (2007) 4430–4443.
[8] S. Kreissl, K. Maute, Levelset based fluid topology optimization using the extended finite element method, Struct. Multidiscip. Optim. 46 (2012) 311–326.
[9] J. Alexandersen, A detailed introduction to density-based topology optimisation of fluid flow problems with implementation in MATLAB, Struct. Multidiscip. Optim. 66 (1) (2023) 12.
[10] S. Whitaker, The Forchheimer equation: a theoretical development, Transp. Porous Media 25 (1) (1996) 27–61.
[11] B. Philippi, Y. Jin, Topology optimization of turbulent fluid flow with a sensitive porosity adjoint method (spam), 2015, arXiv preprint arXiv:1512.08445.
[12] X. Li, K. Wu, L. Zhao, X. Fan, Topology optimization of regenerative cooling structures under high Reynolds number flow with variable thermo-physical properties, Appl. Therm. Eng. (2024) 124602.
[13] Y. Tian, R. Gao, Y. Wang, R. Jing, A. Li, X. Dong, X. Hao, A turbulent flow topology optimization method for diverging tee resistance reduction, J. Build. Eng. 97 (2024) 110609.
[14] M.J.B. Theulings, M. Langelaar, F. van Keulen, R. Maas, Towards improved porous models for solid/fluid topology optimization, Struct. Multidiscip. Optim. 66 (6) (2023) 133.
[15] M. Abdelhamid, A. Czekanski, On the calculation of the Brinkman penalization term in density-based topology optimization of fluid-dependent problems, 2023, arXiv preprint arXiv:2302.14156.
[16] K.E. Jensen, Topology optimization of Stokes flow on dynamic meshes using simple optimizers, Comput. & Fluids 174 (2018) 66–77.
[17] C. Lundgaard, J. Alexandersen, M. Zhou, C.S. Andreasen, O. Sigmund, Revisiting density-based topology optimization for fluid-structure-interaction problems, Struct. Multidiscip. Optim. 58 (2018) 969–995.
[18] S. Kreissl, G. Pingen, K. Maute, Topology optimization for unsteady flow, Internat. J. Numer. Methods Engrg. 87 (13) (2011) 1229–1253.
[19] J. Alexandersen, N. Aage, C.S. Andreasen, O. Sigmund, Topology optimisation for natural convection problems, Internat. J. Numer. Methods Fluids 76 (10) (2014) 699–721.
[20] COMSOL Multiphysics® v.6.1, URL: www.comsol.com.
[21] C. Wu, Y. Zhang, Flow topology optimization at high Reynolds numbers based on modified turbulence models, Aerospace 11 (7) (2024) 525.
[22] B.S. Lazarov, O. Sigmund, Filters in topology optimization based on Helmholtz-type differential equations, Internat. J. Numer. Methods Engrg. 86 (6) (2011) 765–781.
[23] G. Hauke, T. Hughes, A unified approach to compressible and incompressible flows, Comput. Methods Appl. Mech. Engrg. 113 (3–4) (1994) 389–395.
[24] G. Hauke, Simple stabilizing matrices for the computation of compressible flows in primitive variables, Comput. Methods Appl. Mech. Engrg. 190 (51–52) (2001) 6881–6893.
[25] T.J. Hughes, M. Mallet, A new finite element formulation for computational fluid dynamics: III. The generalized streamline operator for multidimensional advective-diffusive systems, Comput. Methods Appl. Mech. Engrg. 58 (3) (1986) 305–328.
[26] COMSOL Multiphysics®, CFD Module User's Guide, COMSOL AB, 2022.